Euclid preparation. Improving cosmological constraints using a new multi-tracer method with the spectroscopic and photometric samples

Fabien Dournac, Alain Blanchard, Stéphane Ilić, Brahim Lamine, Isaac Tutusaus Lleixa, A Amara, S Andreon, N Auricchio, H Aussel, M Baldi, et al.

Astronomy & Astrophysics manuscript no. main
April 19, 2024

Euclid preparation. Improving cosmological constraints using a new multi-tracer method with the spectroscopic and photometric samples

Euclid Collaboration: F. Dournac[1], A. Blanchard[⋆1], S. Ilić[2,1], B. Lamine[1], I. Tutusaus[1], A. Amara[3], S. Andreon[4], N. Auricchio[5], H. Aussel[6], M. Baldi[7,5,8], S. Bardelli[5], C. Bodendorf[9], D. Bonino[10], E. Branchini[11,12,4], S. Brau-Nogue[1], M. Brescia[13,14,15], J. Brinchmann[16], S. Camera[17,18,10], V. Capobianco[10], J. Carretero[19,20], S. Casas[21], M. Castellano[22], S. Cavuoti[14,15], A. Cimatti[23], G. Congedo[24], C. J. Conselice[25], L. Conversi[26,27], Y. Copin[28], F. Courbin[29], H. M. Courtois[30], A. Da Silva[31,32], H. Degaudenzi[33], A. M. Di Giorgio[34], J. Dinis[31,32], M. Douspis[35], F. Dubath[33], X. Dupac[27], S. Dusini[36], A. Ealet[28], M. Farina[34], S. Farrens[6], S. Ferriol[28], M. Frailis[37], E. Franceschi[5], S. Galeotta[37], W. Gillard[38], B. Gillis[24], C. Giocoli[5,39], B. R. Granett[4], A. Grazian[40], F. Grupp[9,41], S. V. H. Haugan[42], W. Holmes[43], I. Hook[44], F. Hormuth[45], A. Hornstrup[46,47], P. Hudelot[48], K. Jahnke[49], E. Keihänen[50], S. Kermiche[38], A. Kiessling[43], M. Kilbinger[51], B. Kubik[28], M. Kümmel[41], M. Kunz[52], H. Kurki-Suonio[53,54], S. Ligori[10], P. B. Lilje[42], V. Lindholm[53,54], I. Lloro[55], D. Maino[56,57,58], E. Maiorano[5], O. Mansutti[37], O. Marggraf[59], K. Markovic[43], N. Martinet[60], F. Marulli[61,5,8], R. Massey[62], S. Maurogordato[63], E. Medinaceli[5], S. Mei[64], Y. Mellier[65,48], M. Meneghetti[5,8], E. Merlin[22], G. Meylan[29], M. Moresco[61,5], L. Moscardini[61,5,8], E. Munari[37], S.-M. Niemi[66], J. W. Nightingale[67,68], C. Padilla[19], S. Paltani[33], F. Pasian[37], K. Pedersen[69], W. J. Percival[70,71,72], V. Pettorino[66], S. Pires[6], G. Polenta[73], M. Poncet[74], L. A. Popa[75], L. Pozzetti[5], F. Raison[9], R. Rebolo[76,77], A. Renzi[78,36], J. Rhodes[43], G. Riccio[14], E. Romelli[37], M. Roncarelli[5], E. Rossetti[7], R. Saglia[41,9], D. Sapone[79], P. Schneider[59], A. Secroun[38], G. Seidel[49], M. Seiffert[43], S. Serrano[80,81,82], C. Sirignano[78,36], G. Sirri[8], L. Stanco[36], C. Surace[60], P. Tallada-Crespí[83,20], D. Tavagnacco[37], A. N. Taylor[24], I. Tereno[31,84], R. Toledo-Moreo[85], F. Torradeflot[20,83], E. A. Valentijn[86], L. Valenziano[5,87], T. Vassallo[41,37], A. Veropalumbo[4,12], Y. Wang[88], A. Zacchei[37,89], G. Zamorani[5], J. Zoubian[38], E. Zucca[5], A. Biviano[37,89], M. Bolzonella[5], A. Boucaud[64], E. Bozzo[33], C. Burigana[90,87], C. Colodro-Conde[76], G. De Lucia[37], D. Di Ferdinando[8], J. A. Escartin Vigo[9], R. Farinelli[5], J. Gracia-Carpio[9], G. Mainetti[91], M. Martinelli[22,92], N. Mauri[23,8], C. Neissner[19,20], Z. Sakr[93,1,94], V. Scottez[65,95], M. Tenti[8], M. Viel[89,37,96,97,98], M. Wiesmann[42], Y. Akrami[99,100], V. Allevato[14], S. Anselmi[36,78,101], C. Baccigalupi[96,37,97,89], A. Balaguera-Antolinez[76,77], M. Ballardini[102,5,103], L. Blot[104,101], S. Borgani[105,89,37,97], S. Bruton[106], R. Cabanac[1], A. Calabro[22], G. Canas-Herrera[66,107], A. Cappi[5,63], C. S. Carvalho[84], G. Castignani[5], T. Castro[37,97,89,98], K. C. Chambers[108], S. Contarini[9,61], A. R. Cooray[109], J. Coupon[33], S. Davini[12], B. De Caro[36,78], S. de la Torre[60], G. Desprez[110], A. Díaz-Sánchez[111], S. Di Domizio[11,12], H. Dole[35], S. Escoffier[38], A. G. Ferrari[23,8], P. G. Ferreira[112], I. Ferrero[42], F. Finelli[5,87], L. Gabarra[112], K. Ganga[64], J. García-Bellido[99], E. Gaztanaga[81,80,113], F. Giacomini[8], G. Gozaliasl[114,53], H. Hildebrandt[115], A. Jimenez Munoz[116], J. J. E. Kajava[117,118], V. Kansal[119,120], D. Karagiannis[121,122], C. C. Kirkpatrick[50], L. Legrand[123], G. Libet[74], A. Loureiro[124,125], J. Macias-Perez[116], G. Maggio[37], M. Magliocchetti[34], F. Mannucci[126], R. Maoli[127,22], C. J. A. P. Martins[128,16], S. Matthew[24], L. Maurin[35], R. B. Metcalf[61,5], M. Migliaccio[129,130], P. Monaco[105,37,97,89], C. Moretti[96,98,37,89,97], G. Morgante[5], S. Nadathur[113], Nicholas A. Walton[131], L. Patrizii[8], A. Pezzotta[9], M. Pöntinen[53], V. Popa[75], C. Porciani[59], D. Potter[132], I. Risso[133], P.-F. Rocci[35], M. Sahlén[134], A. G. Sánchez[9], J. A. Schewtschenko[24], A. Schneider[132], E. Sefusatti[37,89,97], M. Sereno[5,8], J. Steinwagner[9], N. Tessore[135], G. Testera[12], R. Teyssier[136], S. Toft[47,137,138], S. Tosi[11,4,12], A. Troja[78,36], M. Tucci[33], J. Valiviita[53,54], D. Vergani[5], and G. Verza[139,140]

(Affiliations can be found after the references)

ABSTRACT

Future data provided by the *Euclid* mission will allow us to better understand the cosmic history of the Universe. A metric of its performance is the figure-of-merit (FoM) of dark energy, usually estimated with Fisher forecasts. The expected FoM has previously been estimated taking into account the two main probes of *Euclid*, namely the three-dimensional clustering of the spectroscopic galaxy sample, and the so-called 3×2 pt signal from the photometric sample (i.e., the weak lensing signal, the galaxy clustering, and their cross-correlation). So far, these two probes have been treated as independent. In this paper, we introduce a new observable given by the ratio of the (angular) two-point correlation function of galaxies from the two surveys. For identical (normalised) selection functions, this observable is unaffected by sampling noise, and its variance is solely controlled by Poisson noise. We present forecasts for *Euclid* where this multi-tracer method is applied and is particularly relevant because the two surveys will

cover the same area of the sky. This method allows for the exploitation of the combination of the spectroscopic and photometric samples. When the correlation between this new observable and the other probes is not taken into account, a significant gain is obtained in the FoM, as well as in the constraints on other cosmological parameters. The benefit is more pronounced for a commonly investigated modified gravity model, namely the γ parametrisation of the growth factor. However, the correlation between the different probes is found to be significant and hence the actual gain is uncertain. We present various strategies for circumventing this issue and still extract useful information from the new observable.

Key words. Cosmology: dark energy – large-scale structure of Universe – cosmological parameters – Methods: statistical

1. Introduction

In recent decades, a large number of observations and studies have been converging on the fact that our Universe is going through a phase of accelerated expansion, visible on cosmological scales. In order to better understand the origin of this cosmic acceleration and the physics of gravity on large scales, wide galaxy surveys such as *Euclid*[1] (Laureijs et al. 2011) rely essentially on two main probes: galaxy clustering, denoted here by GC_{sp} (GC_{ph}) for analyses with spectroscopic (photometric) redshifts; and weak gravitational lensing (WL), also known as cosmic shear. The GC_{sp} and GC_{ph} probes aim at reconstructing the fluctuations of the underlying dark matter density using coordinates and redshifts from the angular and radial positions of galaxies. Different measurements can be done to extract information from this underlying distribution, such as measurements of the baryon acoustic oscillations (BAOs; Eisenstein et al. 2005; Aubourg et al. 2015), or measurements of the redshift-space distortion effects (RSD; Percival & White 2009). Complementary to the clustering probes, galaxy surveys enable WL analyses. They characterise the matter present along the line of sight, which slightly alters the images of galaxies as a function of the gravitational potentials traversed by photons (see, e.g., Kilbinger 2015, for a detailed review). WL analyses not only extract information about the matter content of the Universe, but also about the growth of structure and the physics of gravitational interaction. Stage-IV galaxy surveys, such as *Euclid*, will provide a large amount of data that will enable very precise GC_{sp}, GC_{ph}, and WL analyses (see, e.g., Euclid Collaboration: Blanchard et al. 2020, from hereafter EP:VII).

As shown in EP:VII, the combination of all main probes (GC_{sp}, GC_{ph}, and WL) will lead to the most stringent constraints from future *Euclid* data. The combination of different probes, sensitive to different aspects of how gravity acts in the cosmos, breaks several degeneracies present between the different cosmological parameters and achieves better constraints.

However, such cosmological probes are in general not independent. It was shown in EP:VII that the cross-correlations between GC_{ph} and WL were another important key contributor in the joint analysis of all *Euclid* probes. More precisely, the figure-of-merit (FoM, Albrecht et al. 2006) of the dark energy equation-of-state parameters[2] improves roughly by a factor of 4 when these cross-correlations are included in the analysis. It was also shown in Tutusaus et al. (2020) that a joint analysis of *Euclid* photometric probes accounting for their cross-correlations can significantly improve our knowledge on nuisance parameters, such as the intrinsic alignment of galaxies or the galaxy bias. Cross-correlations between GC_{ph} and WL have been studied for real observations (see, e.g., Abbott et al. 2022) and the future *Euclid* data (Tutusaus et al. 2020). Similarly, there have been several analysis combining spectroscopic and photometric data (see, e.g., Heymans et al. 2021; Sugiyama et al. 2023). However, the full treatment of all cross-correlations between the spectroscopic probe, GC_{sp}, and the photometric probes, taking into account their covariances and the radial information, has been less considered. One of the main reasons is that spectroscopic analyses are usually performed in three-dimensions, while photometric analyses are done in two-dimensions. This difference makes it non-trivial to properly combine the spectroscopic and photometric probes while accounting for their cross-correlations (although several attempts are available in the literature, see, e.g., Passaglia et al. 2017; Wang et al. 2020; Taylor & Markovič 2022). In EP:VII, the authors neglected any correlation between GC_{sp} and the photometric probes. In the case of *Euclid*, another motivation for this choice is that the spectroscopic measurements will be available only at high redshift ($z > 0.9$), therefore reducing their overlap in volume with the photometric probes. In order to be conservative, a pessimistic scenario was further considered in EP:VII where all objects above $z = 0.9$ were removed for GC_{ph} (and their cross-correlations with WL), with the goal of removing any remaining correlation.

In the present analysis we go beyond the results presented in EP:VII by focusing on extracting additional information from the combination of spectroscopic and photometric probes. Without accounting for all the cross-correlations between spectroscopic and photometric observables (which would require a joint modelling of three- and two-dimensional probes), we extract the additional information from the fact that GC_{sp} and GC_{ph} will probe (at least partially) the same volume of the Universe.

To do so, we introduce the ratio of angular correlation functions (or harmonic space power spectra) between the spectroscopic and photometric tracers as an additional observable according to Alimi et al. (1988) who first suggested this type of statistic to get rid of sampling variance. This approach made it possible to implement a multi-tracer approach (Seljak 2009; McDonald & Seljak 2009). Indeed, given the large number density of *Euclid* objects, if tracers are accurately selected we can get rid of the cosmic variance and obtain very precise measurements of these ratios. In practice, this implies that once the bias of one tracer is known, there is effectively almost no uncertainty on the bias of the other tracer. Given this reduction of the number of degrees of freedom, we can significantly improve the *Euclid* forecasts. In the end, this leads to an improvement of the FoM ranging from 5 % up to 60 %, compared to the baseline analysis presented in EP:VII. The specific improvement depends on the settings of the surveys and the cosmological model considered. *Euclid* is an ESA M-class space mission whose main goal is to measure the geometry of the Universe and the growth of structures out to redshift $z \sim 2$, i.e., a look-back time of 10Gyr and beyond. This space telescope, launched on 1st July 2023, carries a near-infrared spectrometer and photometer instrument (Maciaszek et al. 2022, *Euclid*-NISP) and a visible imager (Cropper et al. 2018, *Euclid*-VIS). These two detectors will perform a galaxy survey over an area of about 15 000 deg^2 of the extragalactic sky. *Euclid*-NISP will be able to measure 30 to 50 mil-

⋆ e-mail: alain.blanchard@irap.omp.eu

[1] https://www.euclid-ec.org

[2] We use the alternative definition from Wang (2008) FoM$= \sqrt{\det\left(\tilde{F}_{w_0 w_a}\right)}$, with $\tilde{F}_{w_0 w_a}$ being the marginalised Fisher submatrix for the dark energy equation-of-state parameters.

lion spectroscopic redshifts between 0.9 and 1.8 (Pozzetti et al. 2016), which can be used for GC measurements, while *Euclid*-VIS will measure about 1.5 billion photometric galaxy shapes, enabling weak lensing (WL) observations (see Laureijs et al. 2011, for more details). The huge volume of data provided by *Euclid* will give new insights into the late Universe, especially on the growth and evolution of large-scale cosmic structures and on the expansion history of the Universe, and more generally shed some light on the nature of dark energy (see Amendola et al. 2018).

The paper is organised as follows. We first describe the *Euclid* survey and how we forecast its constraining power for the main cosmological probes in Sect. 2. We then present the cosmological models considered in Sect. 3. In Sect. 4 we introduce our new observable making use of the multi-tracer approach, and clarify in Sect. 5 its implementation in our forecasts. The main results of the analysis are presented in Sect. 6, and we conclude in Sect. 7.

2. The main *Euclid* cosmological probes

In this section we describe how we forecast the constraining power of *Euclid* for its main cosmological probes. We follow closely the recipes presented in EP:VII and, although we provide a self-contained description in this work, we refer the interested reader to EP:VII for all the technical details.

2.1. Spectroscopic probe

Let us first consider the spectroscopic probe of *Euclid*. The main observable for this probe is the observed galaxy power spectrum, which needs a reference cosmology. Following EP:VII we model it as

$$P_{\rm obs}(k_{\rm ref},\mu_{\rm ref};z) = \frac{1}{q_\perp^2(z)\,q_\parallel(z)} \left\{ \frac{\left[b_{\rm sp}\sigma_8(z) + f\sigma_8(z)\mu^2\right]^2}{1+\left[f(z)k\mu\sigma_{\rm p}(z)\right]^2} \right\} \times \frac{P_{\rm dw}(k,\mu;z)}{\sigma_8^2(z)} F_z(k,\mu;z) + P_{\rm s}(z)\,, \quad (1)$$

where σ_8 is the r.m.s. of linear matter fluctuations on scales of $8\,h^{-1}$Mpc, $b_{\rm sp}$ the galaxy bias parameter, f the growth rate, $\sigma_{\rm p}$ is related to the pairwise peculiar velocity and treated as a free nuisance parameter, μ the cosine of the angle between the wave vector, $\boldsymbol{k}$, and the line-of-sight direction, and all $k := k(k_{\rm ref},\mu_{\rm ref})$ and $\mu := \mu(\mu_{\rm ref})$ with

$$k(k_{\rm ref},\mu_{\rm ref}) = \frac{k_{\rm ref}}{q_\perp}\left[1+\mu_{\rm ref}^2\left(\frac{q_\perp^2}{q_\parallel^2}-1\right)\right]^{1/2}, \quad (2)$$

$$\mu(\mu_{\rm ref}) = \mu_{\rm ref}\frac{q_\perp}{q_\parallel}\left[1+\mu_{\rm ref}^2\left(\frac{q_\perp^2}{q_\parallel^2}-1\right)\right]^{1/2}. \quad (3)$$

RSDs are accounted for through the numerator inside the curly bracket in Eq. (1), and the 'finger-of-God' effect through the denominator. The term $P_{\rm dw}$ is the 'de-wiggled' power spectrum, which accounts for the smearing of the BAOs:

$$P_{\rm dw}(k,\mu;z) = P_{\delta\delta}^{\rm lin}(k;z)\,{\rm e}^{-g_\mu k^2} + P_{\rm nw}(k;z)\left(1-{\rm e}^{-g_\mu k^2}\right), \quad (4)$$

where $P_{\rm nw}$ stands for a no-wiggle power spectrum with the same broad band shape as the linear power spectrum, $P_{\delta\delta}^{\rm lin}$, but without the BAO wiggles. We also account for nonlinearities through a nonlinear damping factor

$$g_\mu(k,\mu,z) = \sigma_{\rm v}^2(z)\left\{1-\mu^2+\mu^2[1+f(z)]^2\right\}, \quad (5)$$

with

$$\sigma_{\rm v}^2(z) = \frac{1}{6\pi^2}\int_0^{+\infty} {\rm d}k\; P_{\delta\delta}^{\rm lin}(k,z)\,. \quad (6)$$

We additionally introduce

$$F_z(k,\mu;z) = {\rm e}^{-k^2\mu^2\sigma_r^2(z)}, \quad (7)$$

where $\sigma_r(z) = (1+z)\sigma_z c/H(z)$ accounts for redshift uncertainties and is modelled as in EP:VII. We set $\sigma_z = 10^{-3}$. Moreover, we consider a residual shot-noise $P_{\rm s}$ as a constant nuisance parameter in each redshift bin. Finally, the quantities

$$q_\perp(z) = \frac{r(z)}{r_{\rm ref}(z)}, \quad (8)$$

$$q_\parallel(z) = \frac{H_{\rm ref}(z)}{H(z)}, \quad (9)$$

account for the Alcock-Paczynski effect (Alcock & Paczynski 1979), where $r(z)$ stands for the comoving angular distance and $H(z)$ is the Hubble expansion rate. The quantities indexed by 'ref' refer to the quantities in the reference cosmology required for measurements of the power spectrum in the spectroscopic survey.

2.2. Photometric probes

With respect to the photometric survey, we consider the harmonic-space angular power spectra $C_{ij}^{XY}(\ell)$, with i and j representing two tomographic bins, and X and Y being either $\mathrm{GC_{ph}}$ or WL. Under the extended Limber approximation (LoVerde & Afshordi 2008), these are given by

$$C_{ij}^{XY}(\ell) = c\int_{z_{\rm min}}^{z_{\rm max}} {\rm d}z\,\frac{W_i^X(z)W_j^Y(z)}{H(z)r^2(z)}P_{\delta\delta}(k_\ell,z)\,, \quad (10)$$

where $k_\ell = (\ell+1/2)/r(z)$, and the nonlinear matter power spectrum is represented by $P_{\delta\delta}$.

The remaining ingredients in Eq. (10) are the kernels for $\mathrm{GC_{ph}}$ or WL,

$$W_i^{\mathrm{GC_{ph}}}(z) = b_i^{\rm ph}(z)n_i(z)\frac{H(z)}{c}, \quad (11)$$

$$W_i^{\rm WL}(z) = \frac{3}{2}\Omega_{\rm m,0}\frac{H_0^2}{c^2}(1+z)\,r(z)\int_z^{z_{\rm max}} {\rm d}z' n_i(z')\frac{r(z,z')}{r(z')} + W_i^{\rm IA}(z)\,, \quad (12)$$

with $n_i(z')$ being the normalised number density distribution of galaxies in tomographic bin i, $b_i^{\rm ph}(z)$ the linear galaxy bias in the same bin, and $r(z,z')$ the comoving angular diameter distance of a source at redshift z' seen from an observer at redshift z. We also consider the intrinsic alignment (IA) of galaxies with the extended nonlinear alignment (eNLA) model, as in EP:VII. This corresponds to the kernel

$$W_i^{\rm IA}(k,z) = -\frac{\mathcal{A}_{\rm IA}\,C_{\rm IA}\,\Omega_{\rm m,0}\,\mathcal{F}_{\rm IA}(z)}{D(z)}\frac{H(z)}{c}, \quad (13)$$

with D the growth factor for linear perturbations:

$$\delta(z) = D(z)\,\delta_0\,, \tag{14}$$

normalised to 1 at $z = 0$, and

$$\mathcal{F}_{\rm IA}(z) = (1+z)^{\eta_{\rm IA}}\left[\frac{\langle L\rangle(z)}{L_*(z)}\right]^{\beta_{\rm IA}}\,. \tag{15}$$

The functions $\langle L\rangle(z)$ and $L_*(z)$ are the redshift-dependent mean and the characteristic luminosity of source galaxies as computed from the luminosity function. For the parameters of the IA model, $\eta_{\rm IA}$, $\beta_{\rm IA}$, $C_{\rm IA}$, and $\mathcal{A}_{\rm IA}$, we consider the fiducial values presented in EP:VII. Further details on the eNLA model and the luminosity dependence assumed can be found there.

2.3. Forecast code

In order to compute the observables described in the previous sections and forecast their cosmological power, we consider here the `TotallySAF`[3] code, which relies on `CAMB` (Lewis et al. 2000) to solve the Boltzmann equations. `TotallySAF` has been used previously for forecasting the constraining power of the main cosmological probes of *Euclid* using the Fisher formalism (EP:VII). The same code allows us to forecast both the spectroscopic ($\rm GC_{sp}$) and photometric probes (WL and $\rm GC_{ph}$), as well as their cross-correlations. An important feature of this code is the possibility to specify the number of points in the n-point stencil derivatives and therefore achieve a high level of accuracy, avoiding numerical instabilities in the Fisher forecast (Yahia-Cherif et al. 2021).

3. Cosmological models

In the present study, the cosmological models investigated are the ones described in EP:VII. These models are spatially flat universes filled with cold dark matter and dynamical dark energy. We also considered non-flat models and a modified gravity model. The dynamics of dark energy is described by a time-varying equation-of-state parameter following the popular CPL parameterisation (Chevallier & Polarski 2001; Linder 2005):

$$w(z) = w_0 + w_a\frac{z}{1+z}\,. \tag{16}$$

Five other cosmological parameters enter in the model: the dimensionless Hubble constant h (defined by $H_0 = 100h\,\mathrm{km\,s^{-1}\,Mpc^{-1}}$); the total matter density at the present time $\Omega_{\rm m}$; the dark energy density at the present time $\Omega_{\rm DE}$; the current baryonic matter density $\Omega_{\rm b}$; the spectral index $n_{\rm s}$ of the primordial spectrum of scalar perturbations; and the current amplitude of matter fluctuations as expressed by σ_8 (the r.m.s. of linear matter fluctuations in spheres of $8h^{-1}\,$Mpc radius). For the description of linear matter perturbations in `CAMB` we take into account here the parameterised-post-Friedmann (PPF) framework of Hu & Sawicki (2007), which enables the equation-of-state to cross $w(z) = -1$ without developing instabilities in the perturbation sector.

Extensions of ΛCDM theories may alter the background as well as the perturbation sector. A simple way to investigate this possibility is through the growth index γ, defined as

$$\gamma(z) = \frac{\ln f(z)}{\ln\Omega_{\rm m}(z)}\,,\quad \text{with}\quad \Omega_{\rm m}(z) \equiv \frac{\Omega_{\rm m,0}(1+z)^3H_0^2}{H^2(z)}\,, \tag{17}$$

[3] https://github.com/syahiacherif/TotallySAF_Alpha

and $f(z)$ the growth rate,

$$f(z) \equiv -\frac{\mathrm{d}\ln D(z)}{\mathrm{d}\ln(1+z)}\,. \tag{18}$$

In standard gravity models, the growth factor is well approximated with a constant $\gamma \approx 0.55$, having a weak dependence on Λ (Lahav et al. 1991). Introducing γ as a constant free parameter is a simple way to describe possible departures from the standard model (Linder 2003).

The fiducial case is the standard concordance model, that is, a spatially-flat Universe filled mostly with cold dark matter and a cosmological constant. Our cosmological models are described by the following vector of parameters with their fiducial values coming from EP:VII:

$$\begin{aligned}\boldsymbol{\lambda} &= \{\Omega_{\rm m,0},\,\Omega_{\rm b,0},\,w_0,\,w_a,\,h,\,n_{\rm s},\,\sigma_8,\,\Omega_{\rm DE},\,\gamma\}\\ &= \{0.32,\,0.05,\,-1.0,\,0.0,\,0.67,\,0.96,\,0.816,\,0.68,\,0.55\}\,.\end{aligned} \tag{19}$$

There are also several nuisance parameters. For the photometric sample, these include the three parameters for the intrinsic alignments, $A_{\rm IA}, \eta_{\rm IA}, \beta_{\rm IA}$, and the linear galaxy bias in each tomographic bin. For the spectroscopic sample, we consider the linear galaxy bias parameter and the residual shot noise, $P_{\rm s}$, in each redshift bin.

The sum of neutrino masses is also fixed to 0.06 eV. In the presence of massive neutrinos, the redshift and scale dependence of the linear growth factor differs from the zero-mass case. This effect is taken into account in standard Boltzmann solvers such as `CAMB` (Lewis et al. 2000)or `CLASS` (Lesgourgues 2011). However, given the small neutrino masses considered in this work, we neglect neutrino effects on the growth factor, following the same approach as in EP:VII, for simplicity.

4. The ratio of correlation functions as additional information

The ratio of the correlation functions of two different galaxy samples, also known as the ratio of cross-correlations, is a powerful method to measure the ratio of the galaxy bias of their respective populations (Alimi et al. 1988). Let us consider measuring two galaxy populations, tracers of the matter density field, δ_1 and δ_2. Let us further assume that both tracers are Poisson realizations of the underlying density fields $\delta_i = b_i\delta$, with b_1, b_2 being the large-scale biases of the two tracers. When the two galaxy populations follow the same selection function over the same volume, this ratio is insensitive to the sampling variance and the Poisson noise is the only source of variance. If the selection functions are different but known, an appropriate weighting scheme will achieve the same result. This is the essence of the multi-tracer approach. It can also be applied to RSD and non-gaussianity measurements (Seljak 2009; McDonald & Seljak 2009). This approach can be applied equivalently to the angular correlation functions or the harmonic power spectra of the two galaxy samples (see for instance Tanidis & Camera 2021; Abramo et al. 2022). In the following, we will consider these two populations to be the spectroscopic and photometric populations of the galaxies observed by *Euclid*. However, it is important to have the same selection function in both data sets in order to benefit from the insensitivity to sample variance. Because of this, we will choose the spectroscopic sample by selecting those galaxies in each one of the photometric tomographic bins for which spectroscopic information is available. This is aimed at ensuring that the selection function for both data sets in the new observable will be the same, that is, the photometric selection function.

A weighting scheme could be necessary to properly achieve this goal, which is feasible as long as the selection functions of the samples are known. To ensure that the same galaxies are not used twice, we will assume that the galaxies in the spectroscopic sample have been removed from the photometric sample.

We first denote as $a_{\ell m,\mathrm{sp}}$ ($a_{\ell m,\mathrm{ph}}$) the coefficients of the spherical-harmonic decomposition of the spectroscopic (photometric) galaxy distribution and the corresponding angular power spectrum $C_{\ell m,\mathrm{sp}}$ ($C_{\ell m,\mathrm{ph}}$). In the absence of any Poisson noise, and assuming a linear galaxy bias relation, we have

$$\frac{|a_{\ell m,\mathrm{sp}}|^2}{|a_{\ell m,\mathrm{ph}}|^2} = \frac{C_{\ell,\mathrm{sp}}}{C_{\ell,\mathrm{ph}}} = \left(\frac{b_{\mathrm{sp}}}{b_{\mathrm{ph}}}\right)^2 , \tag{20}$$

where b_{sp} (b_{ph}) stands for the linear galaxy bias of the spectroscopic (photometric) population.

We consider a spectroscopic sample over a finite volume (given by the photometric selection), assumed to be a Poisson realisation of a field with a density n_{sp}, which represents the galaxy surface density of the spectroscopic sample (in inverse steradians), as well as an unbiased estimator $|\widehat{a_{\ell m,\mathrm{sp}}}|^2$ of $|a_{\ell m,\mathrm{sp}}|^2$. Over the same volume, with an identical selection function, we also consider an unbiased estimation of $|a_{\ell m,\mathrm{ph}}|^2$. We can express the ratio o_ℓ of the angular power spectrum of the two populations as an observable quantity, an estimator of which is

$$\widehat{o_\ell} = \frac{1}{2l+1} \sum_m \frac{|\widehat{a_{\ell m,\mathrm{sp}}}|^2}{|\widehat{a_{\ell m,\mathrm{ph}}}|^2} , \tag{21}$$

For the sake of simplicity, we assume that the Poisson noise for the photometric sample can be neglected, as n_{ph} is expected to be much larger than n_{sp} in *Euclid*. This means that the shot noise is assumed to be low compared to the spectrum itself. Appropriate processing may be required for data applications (see for example Tessore (2017)). Its average over Poisson realisations is then

$$\overline{o_\ell} \equiv \langle \widehat{o_\ell} \rangle = \left\langle \frac{\widehat{C_{\ell,\mathrm{sp}}}}{C_{\ell,\mathrm{ph}}} \right\rangle = \frac{\left\langle \widehat{C_{\ell,\mathrm{sp}}} \right\rangle}{C_{\ell,\mathrm{ph}}} = \left(\frac{b_{\mathrm{sp}}}{b_{\mathrm{ph}}}\right)^2 . \tag{22}$$

Since this quantity is a constant independent of the sample, the average (over samples) is also the same (notice that in this expression C_l is the realization on the specific survey and differs from the ensemble average). The variance $\sigma_o^2(\ell)$ of $\widehat{o_\ell}$ can be inferred (see Appendix) :

$$\sigma_o^2(\ell) = \frac{1}{2\ell+1} \left(\frac{4C_{\ell,\mathrm{sp}}}{f_{\mathrm{sky}}\, C_{\ell,\mathrm{ph}}^2\, n_{\mathrm{sp}}} + \frac{2}{f_{\mathrm{sky}}\, C_{\ell,\mathrm{ph}}^2\, n_{\mathrm{sp}}^2} \right) . \tag{23}$$

The parameter f_{sky} represents the fraction of sky observed by *Euclid*. We can thus build an estimator $\hat{O}$ of $\left(\frac{b_{\mathrm{sp}}}{b_{\mathrm{ph}}}\right)^2$ by taking the optimal (inverse-variance weighted) average over all ℓ and m :

$$\hat{O} = \frac{\sum_{\ell=\ell_{\min}}^{\ell_{\max}} \frac{1}{\sigma_o^2(\ell)} \widehat{o_\ell}}{\sum_{\ell=\ell_{\min}}^{\ell_{\max}} \frac{1}{\sigma_o^2(\ell)}} . \tag{24}$$

The values $\ell_{\min}$ and $\ell_{\max}$ depend on the scenario and are specified in Sect. 6.2 in our case. The variance of this new observable $\hat{O}$ can then be written as :

$$\sigma_O^2 = \left(\sum_{\ell=\ell_{\min}}^{\ell_{\max}} \frac{(2\ell+1) C_{\ell,\mathrm{ph}}^2}{1 + 2 n_{sp} C_{\ell,\mathrm{sp}}} \right)^{-1} \frac{2}{f_{\mathrm{sky}} n_{\mathrm{sp}}^2} . \tag{25}$$

It is important to note that we require the same selection function for both the spectroscopic and photometric data sets to cancel out the dependence on sample variance in Eq. (22) and obtain a direct link between this new observable and the ratio of the linear galaxy biases. That being said, we still consider the standard modelling for $\mathrm{GC_{sp}}$ presented in EP:VII and summarized in Sect. 2.1. For example, we include the impact of RSDs and the finger-of-God effect when modelling the spectroscopic probe. In practice, we consider two different spectroscopic selections: the standard one, with narrow redshift bins; and a new one, derived from the photometric selection, with broad bins. We use the former to derive constraints from $\mathrm{GC_{sp}}$, like in EP:VII, while we only consider the latter to constrain the ratio of the linear galaxy biases present in Eq. (22). We rely on two basic approximations in using Eq. (22). The first one is to assume that only the density term is important for galaxy number counts when we consider the broad photometric selection function, as was considered in EP:VII, for simplicity. Although other terms, like RSD might have a non-negligible contribution (see, e.g, Euclid Collaboration: Tanidis et al. 2023), the change in constraining power when including these effects is very small. Therefore, the same justification to neglect these terms for the photometric data set hold for neglecting them for the harmonic power spectra from the spectroscopic data set (with the broad selection function). The second approximation is that we assume that the linear galaxy bias for the spectroscopic sample used in $\mathrm{GC_{sp}}$ (and therefore considering a top-hat selection function) is the same as the linear galaxy bias for the spectroscopic sample used in the new observable XC2, which considers the photometric selection function for the spectroscopic sample, too. In reality, the linear galaxy bias b_{sp} present in Eq. (22) might depend on the selection function and be slightly different compared to the linear galaxy bias that enters Eq. (1) to model the observed power spectra. Given that both the narrow and broad selection function for the spectroscopic data are centred at the same effective redshift, we assume these two parameters to be the same. We have checked that the difference is smaller than 2% in our cases. In practice, a large difference could however be taken into account if necessary by evaluating from the data the ratio of biases for both samples.

5. Introducing the new observable in Fisher forecasts

5.1. Computing the additional Fisher matrix

We recall briefly the Fisher matrix formalism for a given likelihood $\mathcal{L}$ and model parameters vector $\boldsymbol{\lambda} = \{\lambda_i\}$ (typically cosmological parameters) with fiducial values $\lambda_{i,\mathrm{fid}}$. The F_{ij} element (where the indices i and j run over model parameters) of the Fisher matrix F is defined as

$$F_{ij} \equiv \left\langle -\frac{\partial^2 \ln(\mathcal{L})}{\partial\lambda_i \partial\lambda_j}\bigg|_{\lambda=\lambda_{\mathrm{fid}}} \right\rangle , \tag{26}$$

(Ly et al. 2017) where brackets denote an ensemble average over all possible realisations of the observables considered, given our fiducial model. Assuming that the vector of observables follows a Gaussian distribution, with mean μ and covariance C (which

both can depend on the model parameters), the Fisher matrix can be written analytically as

$$F_{ij} = \frac{1}{2}\,\mathrm{tr}\left[\frac{\partial \mathsf{C}}{\partial\lambda_i}\mathsf{C}^{-1}\frac{\partial \mathsf{C}}{\partial\lambda_j}\mathsf{C}^{-1}\right] + \sum_{mn}\frac{\partial\mu_m}{\partial\lambda_i}(\mathsf{C}^{-1})_{mn}\frac{\partial\mu_n}{\partial\lambda_j}\,. \tag{27}$$

We first consider the combination of two probes A and B; as an example, one may consider the spectroscopic probe (A = $\mathrm{GC_{sp}}$) and the combination of photometric galaxy clustering, weak lensing, and their cross-correlation ($B = \mathrm{GC_{ph}} + \mathrm{WL} + \mathrm{XC}$, often referred to as 3×2 pt in the literature). Defining their respective likelihoods as $\mathcal{L}_A = \mathcal{L}(\mathrm{GC_{sp}})$ and $\mathcal{L}_B = \mathcal{L}(\mathrm{GC_{ph}} + \mathrm{WL} + \mathrm{XC})$, and assuming that A and B are not correlated, then the combined likelihood of both probes will simply be given by the product of the individual likelihoods.

The main idea of the present work is to go beyond this simple probe combination by exploiting the fact that the two probes A and B share the same volume. To do so we introduce the observable O, the ratio of correlation functions defined in Sect. 4 through Eq. (24). Assuming that this new observable (with associated likelihood $\mathcal{L}_O$) is also independent of A and B (the role of correlations is discussed in Sect. 6.3), the total likelihood is

$$\mathcal{L}(\mathrm{GC_{sp}} + \mathrm{GC_{ph}} + \mathrm{WL} + \mathrm{XC} + O) = \mathcal{L}_A\,\mathcal{L}_B\,\mathcal{L}_O\,. \tag{28}$$

This new likelihood $\mathcal{L}_O$ is associated with a 'new' data vector of dimension equal to the number of overlapping redshift bins between the spectroscopic and photometric probes. More details are provided in Sect. 6.1 on the binning of the two probes to ensure the same selection function in the case of *Euclid*. In each redshift bin, the mean value $\mu_O = (b_{\rm sp}/b_{\rm ph})^2$ and variance σ^2_O of those new observables are obtained respectively from Eqs. (22) and (25) in Sect. 4. The new contribution F^O_{ij} to the total Fisher matrix can then be computed for each redshift, thanks to Eq. (27),

$$F^O_{ij} = \frac{1}{\sigma^2_O}\left(\frac{\partial\mu_O}{\partial\lambda_i}\frac{\partial\mu_O}{\partial\lambda_j}\right), \tag{29}$$

where we assume that the observable O follows a Gaussian distribution, and that we ignore the dependence of its variance on the cosmological and nuisance parameters.

The mean value μ_O of the observable O does not depend on the cosmological parameters, but on $b_{\rm sp}$ and $b_{\rm ph}$. Therefore, the only nonzero partial derivatives are

$$\frac{\partial\mu_O}{\partial b_{\rm sp}} = \frac{2\,b_{\rm sp}}{b^2_{\rm ph}} \quad \text{and} \quad \frac{\partial\mu_O}{\partial b_{\rm ph}} = -\frac{2\,b^2_{\rm sp}}{b^3_{\rm ph}}\,. \tag{30}$$

As a consequence, the only nonzero elements of F^O reduce to a 2×2 matrix for each redshift bin, given by

$$F^O = \frac{1}{\sigma^2_O}\begin{pmatrix} \left(\frac{\partial\mu_O}{\partial b_{\rm sp}}\right)^2 & \frac{\partial\mu_O}{\partial b_{\rm sp}}\frac{\partial\mu_O}{\partial b_{\rm ph}} \\ \frac{\partial\mu_O}{\partial b_{\rm sp}}\frac{\partial\mu_O}{\partial b_{\rm ph}} & \left(\frac{\partial\mu_O}{\partial b_{\rm ph}}\right)^2 \end{pmatrix} = \frac{1}{\sigma^2_O}\begin{pmatrix} \frac{4b^2_{\rm sp}}{b^4_{\rm ph}} & -\frac{4b^3_{\rm sp}}{b^5_{\rm ph}} \\ -\frac{4b^3_{\rm sp}}{b^5_{\rm ph}} & \frac{4b^4_{\rm sp}}{b^6_{\rm ph}} \end{pmatrix}. \tag{31}$$

More explicitly, the F^O_{11} element of the above matrix will be added to the F_{ij} element of the total Fisher matrix corresponding to the spectroscopic galaxy bias ($\lambda_i = \lambda_j = b_{\rm sp}$). The element F^O_{22} will be added to the element corresponding the photometric galaxy bias ($\lambda_i = \lambda_j = b_{\rm ph}$). Finally, the two remaining elements of this new Fisher matrix will be additional terms in the off-diagonal elements involving both the spectroscopic and photometric galaxy biases ($\{\lambda_i, \lambda_j\} = \{\lambda_j, \lambda_i\} = \{b_{\rm sp}, b_{\rm ph}\}$). We will address in the next section how we can build from an existing Fisher matrix for the main cosmological probes a new matrix with these additional terms. We denote this new way of combining the 2D and 3D probes as XC2, as opposed to XC that will be used to denote the baseline analysis $\mathrm{GC_{sp}}$+$\mathrm{GC_{ph}}$+WL+XC. We assess now the impact of the combination by examining its effects on the FoM.

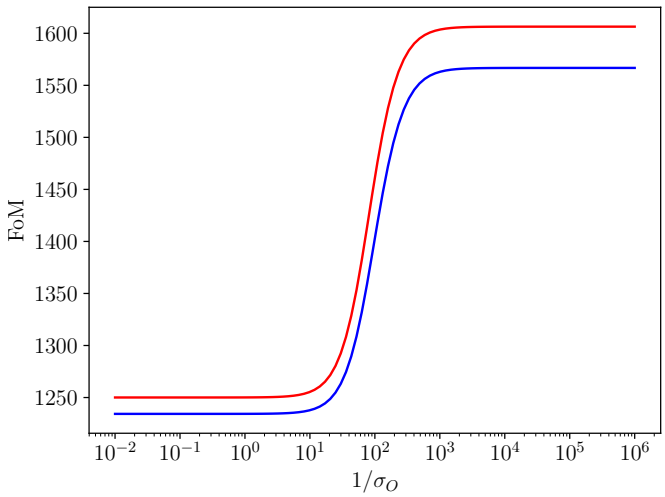

Fig. 1. Evolution of the FoM as a function of the inverse of the standard deviation of the new observable, for the test cases considered in Sect. 5.2. In blue, the case where fiducial values of the spectroscopic biases are taken to be equal to the photometric biases (bottom plateau at FoM=1234 and top plateau at FoM=1567). In red, the case with different fiducial values of the spectroscopic biases and photometric biases following the baseline of EP:VII (bottom plateau at FoM=1250 and top plateau at FoM=1606). The FoM includes the information from $\mathrm{GC_{sp}}$, 3×2 pt, and the new observable.

5.2. Discussion

The objective of the present subsection is to provide an illustration of the benefits from the previously described approach. Firstly, in order to assess the gain obtained by introducing the new observable, we first omit it and compute a baseline FoM, based on the same ingredients and methodology as the optimistic scenario [4] presented in EP:VII. Our only difference is the use of a new redshift binning of the spectroscopic survey to allow for the same effective redshifts for the spectroscopic and the photometric surveys in their overlapping range. The resulting FoM is calculated to be 1250, close to the value of 1257 obtained in EP:VII. Such a minor difference can be explained by the different redshift binning.

Then, to validate our pipeline, a test case is considered where the spectroscopic galaxy bias is set equal to the photometric galaxy bias ($b_{\rm sp} = b_{\rm ph}$).

Next, the new observable O is introduced and its impact on the FoM is assessed. For simplicity, it is assumed that the standard deviation of the new observable, σ_O, remains constant

[4] More details on the settings describing the optimistic scenario are provided in Sect. 6.2.

across all redshift bins (this assumption will be relaxed for the final results in the next section). The value of the FoM with respect to the variation of σ_O is computed and depicted in Fig. 1. When σ_O is large (equivalently, $1/\sigma_O$ is small), the FoM approaches an asymptotic value of 1234. This value is slightly lower than the previously obtained 1250 FoM because the spectroscopic bias has been adjusted to match the photometric bias, resulting in a reduction of constraining power from the spectroscopic sample. Conversely, for a small value of σ_O, the FoM reaches a higher asymptotic value of 1567, indicating that the inclusion of the new observable has a beneficial impact on the FoM. This increase in the FoM for small σ_O is not surprising, as in this scenario, the two tracers essentially share similar values of the galaxy bias with great precision, effectively reducing the total number of degrees of freedom in the problem (i.e., the number of free parameters). Indeed, this asymptotic value of 1567 is recovered numerically using the pipeline used in EP:VII when assuming a common bias, which yields 1567 and thus validates our entire pipeline.

Finally, we conducted tests in which the spectroscopic and photometric galaxy biases were set to their fiducial values as presented in EP:VII ($b_{\rm sp} > b_{\rm ph}$). For scenarios with a large σ_O, we obtained an FoM of 1250, which aligns perfectly with the previously obtained value when the new observable was not included. This result is expected since, for large σ_O, the new observable does not provide additional information. Conversely, for scenarios with a small σ_O, the FoM increased to 1606, showing a similar level of improvement as observed in the previous case with a common bias.

6. Expected improvement on *Euclid* constraints

6.1. Adjustment of the binning and galaxy selection function in the spectroscopic sample

As seen in the previous section, a substantial improvement in constraints can be achieved, provided the variance on the quantity O is small enough. However, this new observable requires that the selection functions for the two samples are identical (up to a normalisation factor). In order to forecast the potential benefits of this method for the *Euclid* constraints, it is necessary to adapt the selection function of the spectroscopic galaxy sample to that of the photometric one, in order to ensure that the former is proportional to the latter.

In practice, for each tomographic bin in the photometric sample, it is necessary to select the galaxies in the spectroscopic sample in such a way that the selection function for the two samples is identical. These selected galaxies will then constitute the corresponding population for the spectroscopic sample in the same redshift bin. Throughout this process, we make the assumption that the selection functions retain an identical form, thus ensuring consistency between the two samples. This objective could in principle be achieved by weighting the galaxies in a given sample by the inverse of the selection function, as long as the latter is known. However, the spatially inhomogeneous nature of the resulting Poisson noise could alter the effectiveness of the method. We note that this new selection function for the spectroscopic sample is only considered for the new observable O, as detailed in Sect. 4. When considering $\mathrm{GC_{sp}}$ we still consider narrow redshift bins,to benefit from the radial precision and include all the relevant effects in the modelling. The only difference for $\mathrm{GC_{sp}}$ compared to EP:VII is that we centre the narrow redshift bins on the effective redshifts of the photometric sample. This allows us to have essentially the same galaxy bias for the spectroscopic galaxies in $\mathrm{GC_{sp}}$ and the new observable.

Table 1 presents the numerical values for the galaxy number density in each bin of the spectroscopic sample. The total density of all five bins adds up to 0.35 galaxies per square arcminute, which corresponds to the density of the entire spectroscopic sample. For the photometric probe, we consider the same binning presented in EP:VII, except for a minor change. Since the spectroscopic survey only goes out to redshift 1.8, we split the last tomographic bin of the photometric sample into two, with half its number density, and therefore consider 11 bins instead of 10. The binning and density values considered for the photometric sample in the redshift range where it overlaps with the spectroscopic sample is presented in Table 2.

Table 1. Expected number density of galaxies for the *Euclid* spectroscopic survey per unit area and redshift intervals, $\mathrm{d}N/\mathrm{d}\Omega\,\mathrm{d}z\left[\mathrm{deg}^{-2}\right]$ for our new set of redshift bins (with respect to the baseline in EP:VII, Table 3) and the corresponding density of galaxies per arcmin^2 for each redshift bin ($n_{\rm gal}$).

Redshift central bin	0.9595	1.087	1.2395	1.45	1.688
$\mathrm{d}N/\mathrm{d}\Omega\,\mathrm{d}z\left[\mathrm{deg}^{-2}\right]$	1807.76	1793.63	1655.01	1320.51	870.13
Δz : width of bin	0.119	0.136	0.169	0.252	0.224
$n_{\rm gal}\left[\mathrm{arcmin}^{-2}\right]$	0.0597	0.0677	0.0781	0.0924	0.0536

Table 2. Expected number density of galaxies for the *Euclid* photometric survey per unit area and redshift intervals, $\mathrm{d}N/\mathrm{d}\Omega\,\mathrm{d}z\left[\mathrm{sr}^{-1}\right]$ for our new set of redshift bins (with respect to the baseline in EP:VII, Table 4) and the corresponding density of galaxies per arcmin^2 for each redshift bin ($n_{\rm gal}$). Only the redshift range that overlaps with the spectroscopic survey is shown.

Redshift central bin	0.9595	1.087	1.2395	1.45	1.688
$\mathrm{d}N/\mathrm{d}\Omega\,\mathrm{d}z\left[\mathrm{sr}^{-1}\right]$	4219063	4821786	5991778	8934486	3970883
Δz : width of bin	0.119	0.136	0.169	0.252	0.224
$n_{\rm gal},\left[\mathrm{arcmin}^{-2}\right]$	3.0	3.0	3.0	3.0	1.5

6.2. Final results

For each redshift bin where data are available from both surveys, we estimate the total Fisher matrix by adding the contribution from the new observable O to the Fisher matrix computed in the standard case. This allows us to monitor the improvement in various *Euclid* constraints coming from our new XC2 cross-correlation probe between photometric and spectroscopic surveys, compared to the case where only the correlation between $\mathrm{GC_{ph}}$ and WL is taken into account (i.e., the 3× 2 pt analysis). We consider two cases in our comparison: the optimistic and the semi-pessimistic cases. In both cases, we start from $\ell_{\rm min} = 10$. For the former, in line with the optimistic case in EP:VII, we apply a cut in multipoles at $\ell_{\rm max} = 5000$ for the weak lensing probe, a cut at $\ell_{\rm max} = 3000$ for $\mathrm{GC_{ph}}$ and XC, and a cut at $k = 0.3h\,\mathrm{Mpc}^{-1}$ for the 3D clustering probe $\mathrm{GC_{sp}}$. For the semi-pessimistic case, the cut is applied at $\ell_{\rm max} = 1500$ for WL, $\ell_{\rm max} = 750$ for $\mathrm{GC_{ph}}$ and XC, and $k = 0.25h\,\mathrm{Mpc}^{-1}$ for $\mathrm{GC_{sp}}$. We note that a linear galaxy bias model will proba-

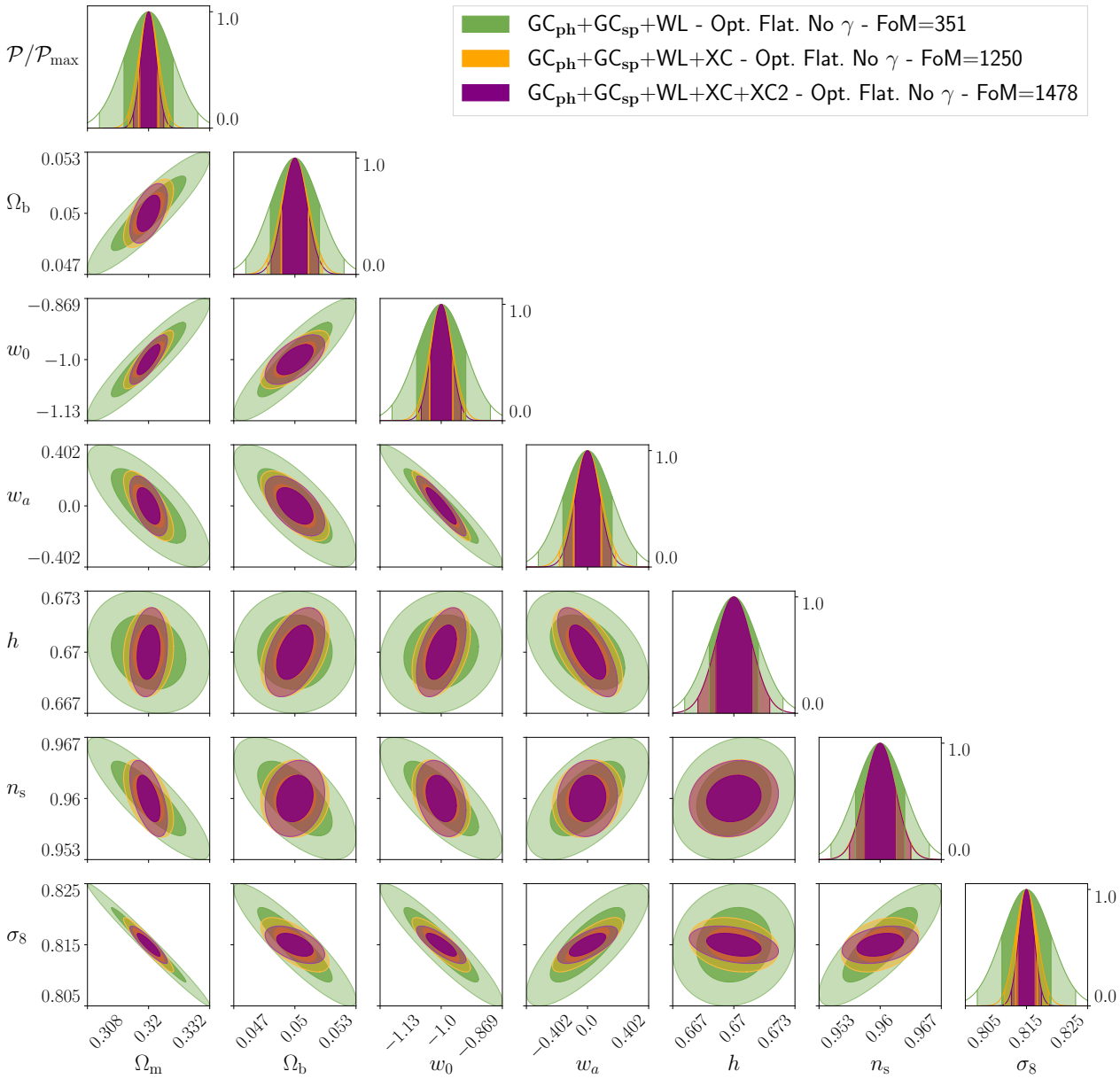

Fig. 2. 1D normalized likelihood ($\mathcal{P}/\mathcal{P}_{max}$) and 2D marginalised Fisher constraints (with 1σ and 2σ limits highlighted) for different combinations of probes. The most stringent constraints are obtained when including the new ratio observable (XC2).

bly break down at the very small scales probed in the optimistic case. If we were to consider a nonlinear galaxy bias model, the link between our new observable and the ratio of galaxy biases from Eq. (22) would change. This might be possible to explore, but the extension to higher-order galaxy bias models is beyond the scope of this work. We still provide the results for the semi-pessimistic scenario, for which a linear galaxy bias model will be more appropriate, and decide to show the results for the optimistic case to compare with the ones presented in EP:VII. Figure 2 shows the marginalised constraints for the cosmological parameters in the optimistic case of the (w_0, w_a) scenario. The addition of the new observable (XC2) clearly improves the constraints and modifies the orientation of correlation ellipses between some parameters, hinting at a breaking of degeneracies. Similar comparisons are performed and illustrated in Fig. 3 for the case where the growth index γ is left free. Although no specific behaviour emerges from this comparison, we notice that a degeneracy between σ_8 and γ appears when adding the new observable XC2. The improvement on the individual cosmological parameters are summarised in Fig. 4. This provides a visual comparison of the relative errors on each cosmological parameter and the corresponding FoM for all the cases studied. Although the XC2 method always leads to appreciable improvements, it seems that no regular behaviour can be identified, as some parameters are improved for some cases and not for others.

The gains on the FoM are summarised in Table 3 for the semi-pessimistic and optimistic scenarios, with a flat or non-flat cosmology, within general relativity. For the modified gravity case through the γ model, the comparison of FoMs is presented in Table 4. The percentages correspond to the relative improvement on constraints provided by the XC2 method compared to the baseline analysis. In the case of general relativity, the FoM exhibits gains ranging from 18% to 25%. However, when considering cases with γ, substantial gains are observed for both the semi-pessimistic and optimistic scenarios in the flat case. The FoM increases by up to 54% for the semi-pessimistic case and

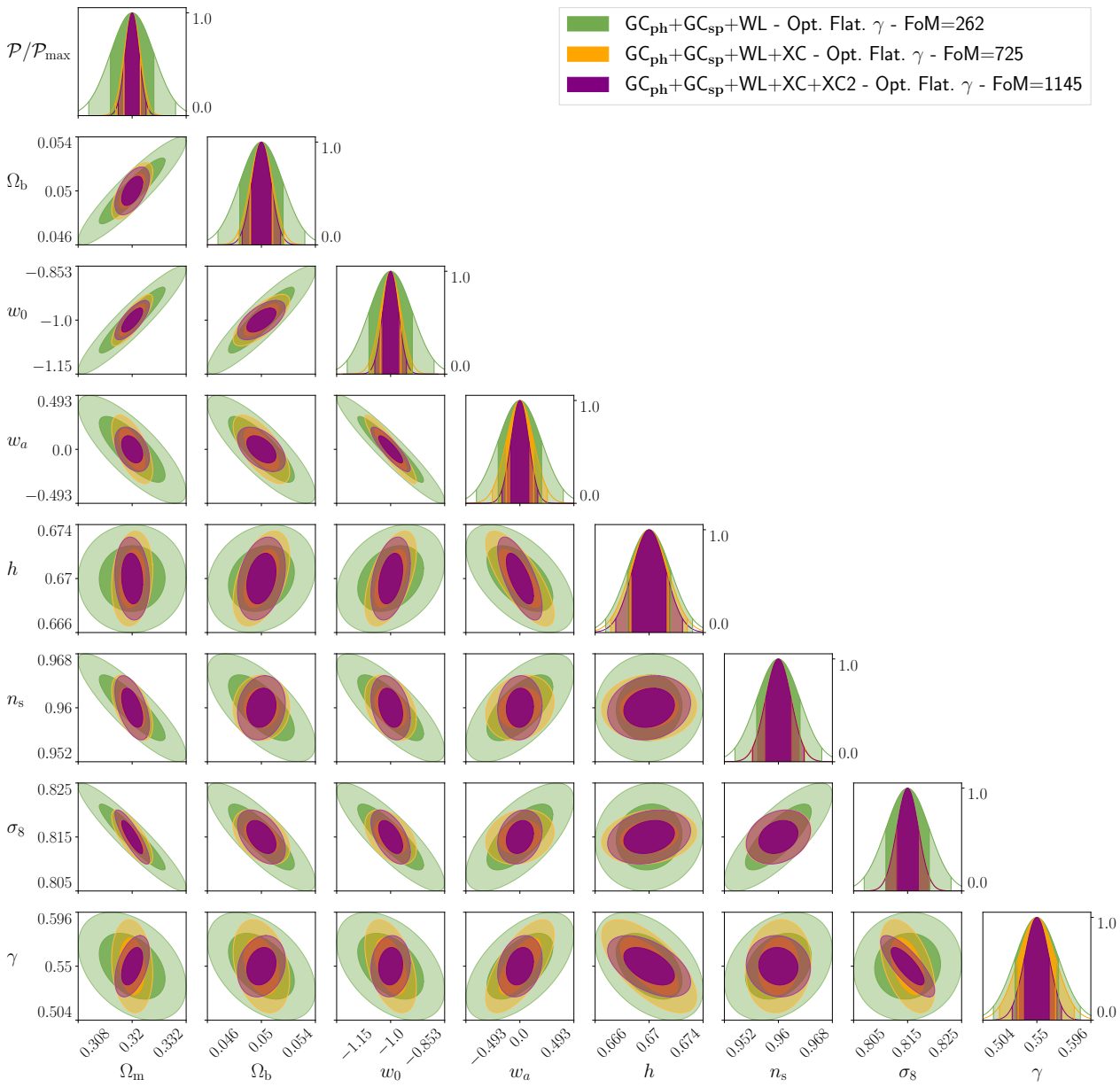

Fig. 3. Same as in Fig. 2 for the modified gravity scenario, with the growth index γ as additional parameter.

57% for the optimistic case. In contrast, for the non-flat case with γ, the increase is only 21%. Interestingly, the improvements on the FoM are highest for the flat cosmological case with the modified gravity γ model. We also emphasise that a significant improvement is obtained on γ, by a factor that seems to be roughly the same regardless of the scenario considered. This suggests that the XC2 probe is well-suited to bring interesting constraints for modified gravity models.

6.3. Taking into account correlations

The results of previous sections were obtained assuming vanishing cross-correlations between O and the C_ℓ. Such terms would appear in the non-diagonal part of the covariance matrix. We have, therefore, evaluated the correlation coefficient κ_ℓ between the two observables o_ℓ (Eq. 21) and $C_{\ell,\mathrm{sp}}$:

$$\kappa_\ell = \frac{\left\langle (\hat{o}_\ell - \bar{o}_\ell)\left(\widehat{C_{\ell,\mathrm{sp}}} - \overline{C_{\ell,\mathrm{sp}}}\right)\right\rangle}{\sigma_o\,\sigma_C}, \tag{32}$$

in which σ_C^2 stands for the variance of the $\widehat{C_{\ell,\mathrm{sp}}}$, which is given by

$$\sigma_C = \sqrt{\frac{2}{(2\ell+1)f_{\mathrm{sky}}}\left(\overline{C_{\ell,\mathrm{sp}}} + \frac{1}{n_{\mathrm{sp}}}\right)}. \tag{33}$$

The correlation coefficient κ_ℓ has been estimated accordingly to Eq. (32) and is plotted against ℓ in Fig. 5. Clearly the coefficient κ_ℓ is significant on all scales. The high correlation may undermine the effectiveness of the multi-tracer method as outlined in its simplified version above. On the other hand, employing suitable weighting schemes may help mitigate this degradation (Seljak et al. 2009; Hamaus et al. 2010), but this is beyond the scope of this paper.

6.4. Further strategies for our multi-tracer method.

In order to see whether our method could still be useful, we have studied different strategies to get around the difficulty resulting

Table 3. FoM values with (XC2) and without (XC) the new observable O, and the corresponding relative improvement, for both the semi-pessimistic and optimistic scenarios, in flat and non-flat cosmologies, assuming general relativity. Improvements are less important when the cut on ℓ for the new observable is lower, but there is still a significant improvement, especially in the semi-pessimistic case.

General relativity				
Cut on ℓ for O	Scenario	Curvature	FoM - XC2/XC	Gain
ℓ = 3000	Optimistic	Flat	1477.5/1250	+18.2%
		Non-Flat	608.6/485	+25.5%
ℓ = 750	Semi-Pessimistic	Flat	689.9/567.6	+21.5%
		Non-Flat	181.7/145.5	+24.9%
ℓ = 300	Optimistic	Flat	1413.4/1250	+13.1%
		Non-Flat	572.3/485	+18%
	Semi-Pessimistic	Flat	678.6/567.6	+19.6%
		Non-Flat	177.2/145.5	+21.8%
	Cut on all probes	Flat	423.1/241.7	+75.1%
		Non-Flat	151.1/93.7	+61.3%
ℓ = 100	Optimistic	Flat	1318.7/1250	+5.5%
		Non-Flat	521.1/485	+7.4%
	Semi-Pessimistic	Flat	637.2/567.6	+12.3%
		Non-Flat	164.1/145.5	+12.8%
	Cut on all probes	Flat	154.8/89.5	+73%
		Non-Flat	58.9/37.4	+57.5%

Table 4. FoM values with (XC2) and without (XC) the new observable O, and the corresponding relative improvement, for both the semi-pessimistic and optimistic scenarios, in flat and non-flat cosmologies, assuming modified gravity. Improvements are less important when the cut on ℓ for the new observable is lower, but there is still a significant improvement, especially in the semi-pessimistic case.

Modified gravity				
Cut on ℓ for O	Scenario	Curvature	FoM - XC2/XC	Gain
ℓ = 3000	Optimistic	Flat	1144.5/725.1	+57.8%
		Non-Flat	565.2/464.4	+21.7%
ℓ = 750	Semi-Pessimistic	Flat	516.5/334.2	+54.5%
		Non-Flat	171.4/140.9	+21.6%
ℓ = 300	Optimistic	Flat	1054.2/725.1	+45.4%
		Non-Flat	548.7/464.4	+18.2%
	Semi-Pessimistic	Flat	503.9/334.2	+50.8%
		Non-Flat	168.7/140.9	+19.7%
	Cut on all probes	Flat	332.9/183.6	+81.3%
		Non-Flat	127.6/92.6	+37.8%
ℓ = 100	Optimistic	Flat	886.9/725.1	+22.3%
		Non-Flat	521/464.4	+12.2%
	Semi-Pessimistic	Flat	453.2/334.2	+35.6%
		Non-Flat	160.9/140.9	+14.2%
	Cut on all probes	Flat	139.9/87.85	+59.3%
		Non-Flat	45/33.2	+35.5%

from these strong correlations. In the first strategy, we assume that a fraction of the survey is devoted to the standard combination of probes in our XC2 synthesis, while the other part $1 - \alpha$ of the survey is used only for the determination of the observable O. In such a configuration, it is reasonable to assume that the volumes for each observable are independent and therefore O is not correlated to the other probes. The FoM obtained with this strategy is represented by the blue curves in Figs. 6 and 7,

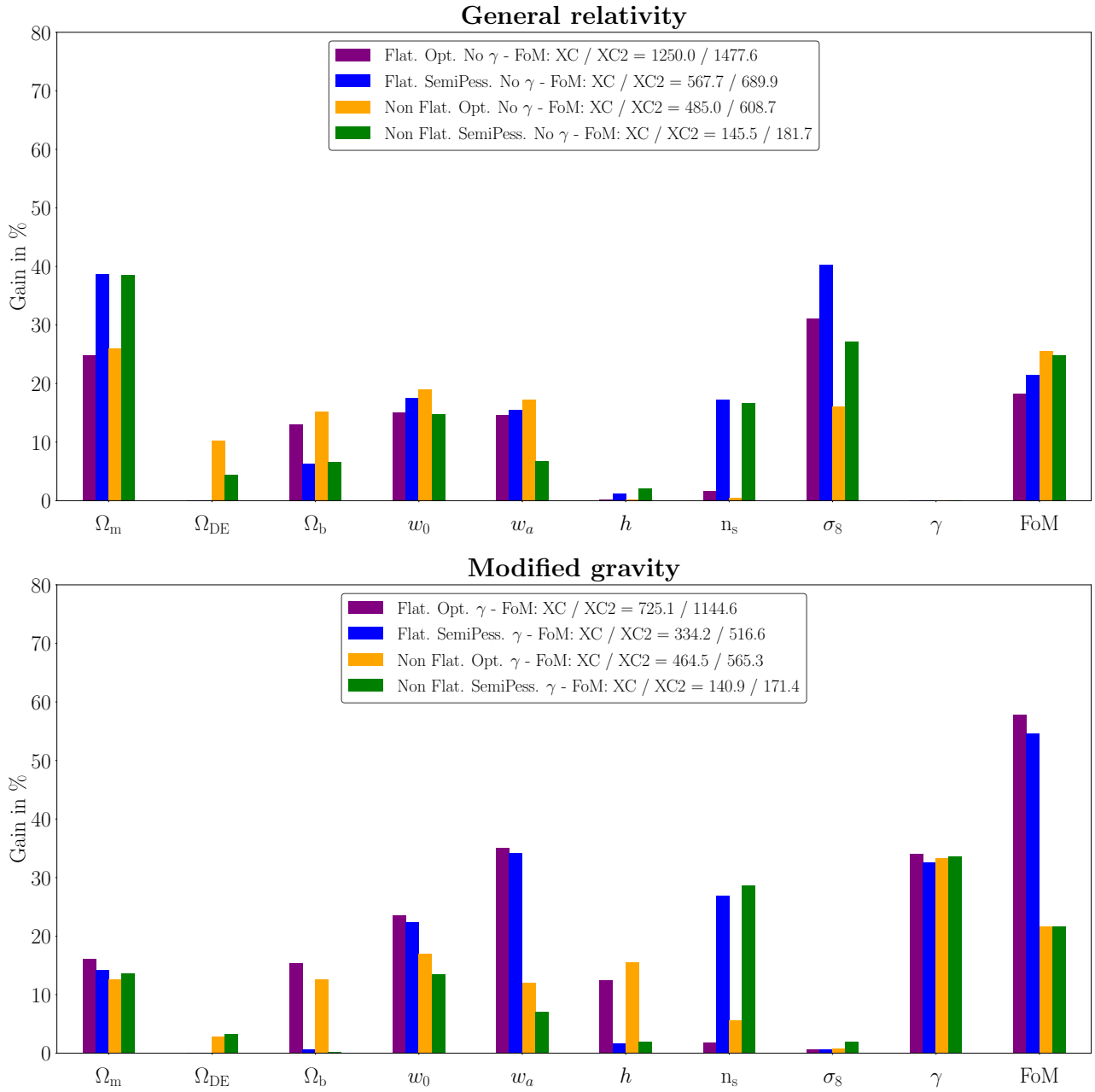

Fig. 4. Improvement on cosmological constraints from adding the new observable XC2 compared to the baseline analysis. The top panel shows the improvement for the semi-pessimistic and optimistic settings, and flat and non-flat cosmologies within general relativity. The bottom panel shows the equivalent figure for the modified gravity scenario including the growth index γ.

where we have considered the optimistic settings. While in the standard scenario (Fig. 6), this strategy does not lead to any improvement in the FoM, one can see from Fig. 7 some gain can be obtained in the modified gravity γ model. In more detail, by devoting 87 % of the sky coverage to the standard combination of probes and 13 % to the computation of the new observable, the FoM is 9.4 % higher with our multi-tracer approach. This improvement is modest compared to the 58% obtained in Table 4, but it demonstrates that our method can still provide additional information.

In the second strategy, we assume that the 3×2 pt analysis is kept for the full survey, while only a fraction α is used for the GC_{sp} analysis and $(1-\alpha)$ for the observable O. This case is represented by the orange curve in Figs. 6 and 7. In the standard model, a modest but non-zero improvement can be seen (4.4%) when 71 % of the survey area is used for GC_{sp} and 29 % is used for the new observable. This improvement is more appreciable in the the γ model with a 30 % improvement for $\alpha = 0.57$.

In the final strategy, we assume that the observable O is derived from an independent survey. This assumption necessitates a thorough understanding and mastery of the (photometric) selection functions for the GC_{sp} and GC_{ph} surveys. The use of an independent survey then becomes feasible for accessing the observable O. For instance, in the Legacy Survey of Space and Time (LSST) of the Vera C. Rubin Observatory, a significant portion of the observed sky will overlap with the *Euclid* sur-

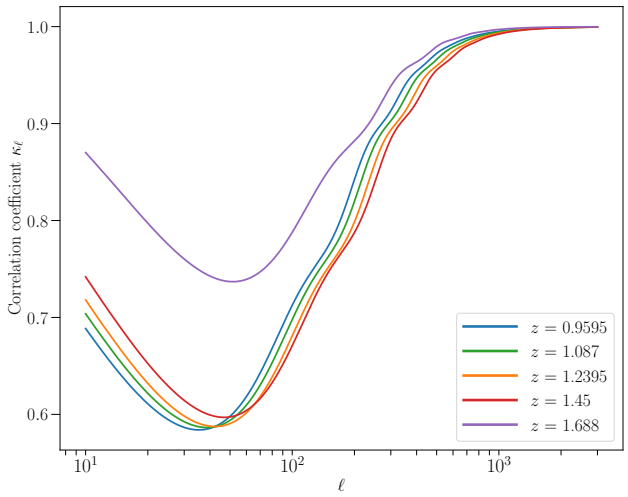

Fig. 5. Correlation coefficient κ_ℓ as a function of ℓ

vey. This, in principle, should enable a precise understanding of the (photometric) selection functions employed in *Euclid* (GC_{sp} and GC_{ph}). Subsequently, the portion of the LSST survey not covered by *Euclid* can be utilized to estimate the observable O. This case is exemplified by the green curves in Figs. 6 and 7. As one can observe, a significant enhancement is achieved even for $\alpha \simeq 0.2-0.3$. The improvement is consistently more pronounced in the case of the γ model, suggesting that our multi-tracer approach yields a more substantial benefit in the context of modified gravity theories. However, it is important to note that the expected gain should be evaluated on a case-by-case basis. We note that for this last strategy we consider values of α up to 1.2. This illustrates the improvement on the FoM when using an independent survey with a sky coverage even up to 20 % larger than *Euclid*.

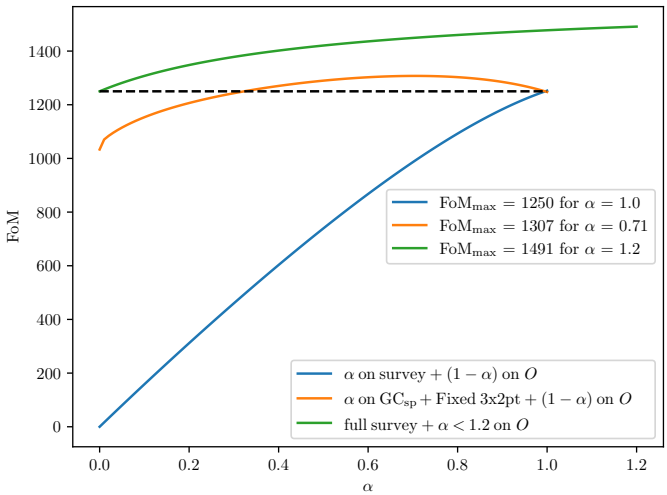

Fig. 6. Figure-of-Merit (FoM) as a function of the fraction α of Euclid's observed sky (f_{sky}). The blue curve represents the combination of a fraction α for the main probes (GC_{sp} and 3x2pt) and $(1-\alpha)$ for the new observable O. The orange curve represents the combination of a fraction of α for GC_{sp}, together with the full 3x2pt analysis for the full survey and a contribution of $(1-\alpha)$ for the new observable O. The green curve shows the FoM of the full survey with an additional external contribution from the new observable up to a factor $\alpha = 1.2$. The dashed line represents the optimal FoM using the standard GC_{sp} and 3x2pt analysis. See the text for additional details on the different cases.

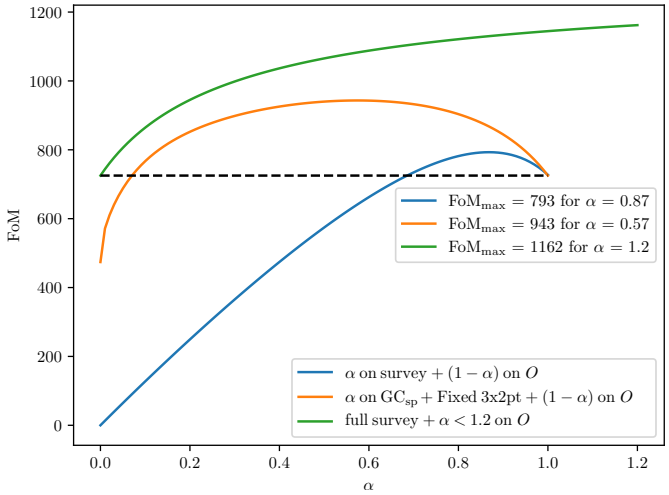

Fig. 7. Figure-of-Merit (FoM) as a function of the fraction α of Euclid's observed sky (f_{sky}). We consider here the modified gravity model with the γ parameter. The different curves correspond to the same cases treated in Fig 6.

7. Conclusions

Spectroscopic galaxy surveys provide information on both the geometrical distribution of galaxies and their dynamics (through RSDs). Photometric galaxy surveys provide information on both the geometrical distribution of the tracers and the distribution of dark matter through its weak lensing imprint on the shape of galaxies. The information that can be inferred from a survey of a single tracer is primarily limited by the finite volume of the sample, i.e., the sampling noise. In the upcoming generation of wide-field surveys, there will be a significant overlap in the footprint of those two categories of survey. In the case of *Euclid*, the the area overlap between the spectroscopic survey and the photometric survey will be nearly 100%. This overlap offers the opportunity to bring additional information via cross-correlations. Euclid Collaboration: Paganin et al. (in prep.) address the issue of the joint use of the 2D and 3D surveys in *Euclid*, including their cross-correlations as an additional data vector. Their conclusion is that the covariance between 2D and 3D data can be safely neglected and the addition of the 2D×3D data vector does not significantly change the final constraints. However, when two tracers are available over the same volume, one can also infer the ratio of the bias of the two populations without being limited by the sampling noise (Alimi et al. 1988; Seljak 2009). Given the large number density of objects that will be observed by the upcoming surveys, the Poisson noise limitation is expected to be very small. In this paper, we have introduced a new observable quantity, the ratio of angular (cross-)correlation functions, which provides an additional data vector, enabling a simple implementation of the multi-tracer technique. Using the specifications of *Euclid*, we have shown that this additional observable provides useful information, resulting in improved estimations of cosmological parameters and, thereby, the FoM of dark energy. Depending on the settings, this improvement can vary from modest (5%) to more substantial (up to 60%). It therefore appears to be a promising approach for enhancing the constraints from future joint analyses when two probes sample the same volume. Interestingly, a gain is achievable even when the biases of the two probes are identical. The details of this gain do not seem to follow a regular pattern. While it leads to a clear improvement in the FoM, constraints on certain cosmological parameters are

contingent upon the specific cases studied. For instance, in the general relativity case, no significant enhancement is observed in the constraint on the Hubble parameter, whereas an improvement is observed within the γ model. The constraints on the main targeted parameters, namely the FoM and constraint on γ, consistently exhibit improvement across the various cases investigated. We conclude that the actual benefit of this method needs to be assessed on a case-by-case basis. Finally, we note that the new additional observable we introduced is strongly correlated with the GC_{sp} harmonic power spectra. However, we have proposed different strategies, namely splitting the survey into two smaller surveys, or using an independent external survey, to circumvent such a large correlation. With these strategies we show that the multi-tracer technique proposed in this work can still provide additional valuable information from the combination of probes.

Acknowledgements. S. Ilić thanks the Centre national d'études spatiales (CNES) which supports his postdoctoral research contract. The Euclid Consortium acknowledges the European Space Agency and a number of agencies and institutes that have supported the development of *Euclid*, in particular the Academy of Finland, the Agenzia Spaziale Italiana, the Belgian Science Policy, the Canadian Euclid Consortium, the French Centre National d'Etudes Spatiales, the Deutsches Zentrum für Luft- und Raumfahrt, the Danish Space Research Institute, the Fundação para a Ciência e a Tecnologia, the Ministerio de Ciencia e Innovación, the National Aeronautics and Space Administration, the National Astronomical Observatory of Japan, the Netherlandse Onderzoekschool Voor Astronomie, the Norwegian Space Agency, the Romanian Space Agency, the State Secretariat for Education, Research and Innovation (SERI) at the Swiss Space Office (SSO), and the United Kingdom Space Agency. A complete and detailed list is available on the *Euclid* web site (`http://www.euclid-ec.org`)..

References

Abbott, T. M. C., Aguena, M., Alarcon, A., et al. 2022, Phys. Rev. D, 105, 023520
Abramo, L. R., Dinarte Ferri, J. V., Tashiro, I. L., & Loureiro, A. 2022, J. Cosmology Astropart. Phys., 8, 073
Albrecht, A., Bernstein, G., Cahn, R., et al. 2006, arXiv e-prints, arXiv:0609591
Alcock, C. & Paczynski, B. 1979, Nature, 281, 358
Alimi, J. M., Valls-Gabaud, D., & Blanchard, A. 1988, A&A, 206, L11
Amendola, L., Appleby, S., Avgoustidis, A., et al. 2018, Living Reviews in Relativity, 21, 2
Aubourg, É., Bailey, S., Bautista, J. E., et al. 2015, Phys. Rev. D, 92, 123516
Chevallier, M. & Polarski, D. 2001, Int. J. Mod. Phys., D10, 213
Cropper, M., Pottinger, S., Azzollini, R., et al. 2018, in Space Telescopes and Instrumentation 2018: Optical, Infrared, and Millimeter Wave, ed. M. Lystrup, H. A. MacEwen, G. G. Fazio, N. Batalha, N. Siegler, & E. C. Tong, Vol. 10698, International Society for Optics and Photonics (SPIE), 709 – 729
Eisenstein, D. J., Zehavi, I., Hogg, D. W., et al. 2005, ApJ, 633, 560
Euclid Collaboration: Blanchard, A., Camera, S., Carbone, C., et al. 2020, A&A, 642, A191
Euclid Collaboration: Tanidis, K., Cardone, V. F., Martinelli, M., et al. 2023, arXiv e-prints, arXiv:2309.00052
Hamaus, N., Seljak, U., Desjacques, V., Smith, R. E., & Baldauf, T. 2010, Phys. Rev. D, 82, 043515
Heymans, C., Tröster, T., Asgari, M., et al. 2021, A&A, 646, A140
Hu, W. & Sawicki, I. 2007, Phys. Rev. D, 76, 104043
Kilbinger, M. 2015, Rep. Prog. Phys., 78, 086901
Lahav, O., Lilje, P. B., Primack, J. R., & Rees, M. J. 1991, MNRAS, 251, 128
Laureijs, R., Amiaux, J., Arduini, S., et al. 2011, arXiv:1110.3193
Lesgourgues, J. 2011, arXiv e-prints, arXiv:1104.2932
Lewis, A., Challinor, A., & Lasenby, A. 2000, ApJ, 538, 473
Linder, E. V. 2003, Phys. Rev. Lett., 90, 091301
Linder, E. V. 2005, Phys. Rev. D, 72, 043529
LoVerde, M. & Afshordi, N. 2008, Phys. Rev. D, 78, 123506
Ly, A., Marsman, M., Verhagen, J., Grasman, R., & Wagenmakers, E.-J. 2017, arXiv e-prints, arXiv:1705.01064
Maciaszek, T., Ealet, A., Gillard, W., et al. 2022, in Society of Photo-Optical Instrumentation Engineers (SPIE) Conference Series, Vol. 12180, Space Telescopes and Instrumentation 2022: Optical, Infrared, and Millimeter Wave, ed. L. E. Coyle, S. Matsuura, & M. D. Perrin, 121801K
McDonald, P. & Seljak, U. 2009, J. Cosmology Astropart. Phys., 10, 007
Passaglia, S., Manzotti, A., & Dodelson, S. 2017, Phys. Rev. D, 95, 123508
Percival, W. J. & White, M. 2009, MNRAS, 393, 297
Pozzetti, L., Hirata, C. M., Geach, J. E., et al. 2016, A&A, 590, A3
Seljak, U. 2009, Phys. Rev. Lett., 102, 021302
Seljak, U., Hamaus, N., & Desjacques, V. 2009, Phys. Rev. Lett., 103, 091303
Sugiyama, S., Miyatake, H., More, S., et al. 2023, arXiv e-prints, arXiv:2304.00705
Tanidis, K. & Camera, S. 2021, MNRAS, 502, 2952
Taylor, P. L. & Markovič, K. 2022, Phys. Rev. D, 106, 063536
Tessore, N. 2017, MNRAS, 471, L57
Tutusaus, I., Martinelli, M., Cardone, V. F., et al. 2020, A&A, 643, A70
Wang, M. S., Avila, S., Bianchi, D., Crittenden, R., & Percival, W. J. 2020, J. Cosmology Astropart. Phys., 10, 022
Wang, Y. 2008, Phys. Rev. D, 77, 123525
Yahia-Cherif, S., Blanchard, A., Camera, S., et al. 2021, A&A, 649, A52

[1] Institut de Recherche en Astrophysique et Planétologie (IRAP), Université de Toulouse, CNRS, UPS, CNES, 14 Av. Edouard Belin, 31400 Toulouse, France
[2] Université Paris-Saclay, CNRS/IN2P3, IJCLab, 91405 Orsay, France
[3] School of Mathematics and Physics, University of Surrey, Guildford, Surrey, GU2 7XH, UK
[4] INAF-Osservatorio Astronomico di Brera, Via Brera 28, 20122 Milano, Italy
[5] INAF-Osservatorio di Astrofisica e Scienza dello Spazio di Bologna, Via Piero Gobetti 93/3, 40129 Bologna, Italy
[6] Université Paris-Saclay, Université Paris Cité, CEA, CNRS, AIM, 91191, Gif-sur-Yvette, France
[7] Dipartimento di Fisica e Astronomia, Università di Bologna, Via Gobetti 93/2, 40129 Bologna, Italy
[8] INFN-Sezione di Bologna, Viale Berti Pichat 6/2, 40127 Bologna, Italy
[9] Max Planck Institute for Extraterrestrial Physics, Giessenbachstr. 1, 85748 Garching, Germany
[10] INAF-Osservatorio Astrofisico di Torino, Via Osservatorio 20, 10025 Pino Torinese (TO), Italy
[11] Dipartimento di Fisica, Università di Genova, Via Dodecaneso 33, 16146, Genova, Italy
[12] INFN-Sezione di Genova, Via Dodecaneso 33, 16146, Genova, Italy
[13] Department of Physics "E. Pancini", University Federico II, Via Cinthia 6, 80126, Napoli, Italy
[14] INAF-Osservatorio Astronomico di Capodimonte, Via Moiariello 16, 80131 Napoli, Italy
[15] INFN section of Naples, Via Cinthia 6, 80126, Napoli, Italy
[16] Instituto de Astrofísica e Ciências do Espaço, Universidade do Porto, CAUP, Rua das Estrelas, PT4150-762 Porto, Portugal
[17] Dipartimento di Fisica, Università degli Studi di Torino, Via P. Giuria 1, 10125 Torino, Italy
[18] INFN-Sezione di Torino, Via P. Giuria 1, 10125 Torino, Italy
[19] Institut de Física d'Altes Energies (IFAE), The Barcelona Institute of Science and Technology, Campus UAB, 08193 Bellaterra (Barcelona), Spain
[20] Port d'Informació Científica, Campus UAB, C. Albareda s/n, 08193 Bellaterra (Barcelona), Spain
[21] Institute for Theoretical Particle Physics and Cosmology (TTK), RWTH Aachen University, 52056 Aachen, Germany
[22] INAF-Osservatorio Astronomico di Roma, Via Frascati 33, 00078 Monteporzio Catone, Italy
[23] Dipartimento di Fisica e Astronomia "Augusto Righi" - Alma Mater Studiorum Università di Bologna, Viale Berti Pichat 6/2, 40127 Bologna, Italy
[24] Institute for Astronomy, University of Edinburgh, Royal Observatory, Blackford Hill, Edinburgh EH9 3HJ, UK
[25] Jodrell Bank Centre for Astrophysics, Department of Physics and Astronomy, University of Manchester, Oxford Road, Manchester M13 9PL, UK
[26] European Space Agency/ESRIN, Largo Galileo Galilei 1, 00044 Frascati, Roma, Italy
[27] ESAC/ESA, Camino Bajo del Castillo, s/n., Urb. Villafranca del Castillo, 28692 Villanueva de la Cañada, Madrid, Spain

[28] Université Claude Bernard Lyon 1, CNRS/IN2P3, IP2I Lyon, UMR 5822, Villeurbanne, F-69100, France
[29] Institute of Physics, Laboratory of Astrophysics, Ecole Polytechnique Fédérale de Lausanne (EPFL), Observatoire de Sauverny, 1290 Versoix, Switzerland
[30] UCB Lyon 1, CNRS/IN2P3, IUF, IP2I Lyon, 4 rue Enrico Fermi, 69622 Villeurbanne, France
[31] Departamento de Física, Faculdade de Ciências, Universidade de Lisboa, Edifício C8, Campo Grande, PT1749-016 Lisboa, Portugal
[32] Instituto de Astrofísica e Ciências do Espaço, Faculdade de Ciências, Universidade de Lisboa, Campo Grande, 1749-016 Lisboa, Portugal
[33] Department of Astronomy, University of Geneva, ch. d'Ecogia 16, 1290 Versoix, Switzerland
[34] INAF-Istituto di Astrofisica e Planetologia Spaziali, via del Fosso del Cavaliere, 100, 00100 Roma, Italy
[35] Université Paris-Saclay, CNRS, Institut d'astrophysique spatiale, 91405, Orsay, France
[36] INFN-Padova, Via Marzolo 8, 35131 Padova, Italy
[37] INAF-Osservatorio Astronomico di Trieste, Via G. B. Tiepolo 11, 34143 Trieste, Italy
[38] Aix-Marseille Université, CNRS/IN2P3, CPPM, Marseille, France
[39] Istituto Nazionale di Fisica Nucleare, Sezione di Bologna, Via Irnerio 46, 40126 Bologna, Italy
[40] INAF-Osservatorio Astronomico di Padova, Via dell'Osservatorio 5, 35122 Padova, Italy
[41] Universitäts-Sternwarte München, Fakultät für Physik, Ludwig-Maximilians-Universität München, Scheinerstrasse 1, 81679 München, Germany
[42] Institute of Theoretical Astrophysics, University of Oslo, P.O. Box 1029 Blindern, 0315 Oslo, Norway
[43] Jet Propulsion Laboratory, California Institute of Technology, 4800 Oak Grove Drive, Pasadena, CA, 91109, USA
[44] Department of Physics, Lancaster University, Lancaster, LA1 4YB, UK
[45] Felix Hormuth Engineering, Goethestr. 17, 69181 Leimen, Germany
[46] Technical University of Denmark, Elektrovej 327, 2800 Kgs. Lyngby, Denmark
[47] Cosmic Dawn Center (DAWN), Denmark
[48] Institut d'Astrophysique de Paris, UMR 7095, CNRS, and Sorbonne Université, 98 bis boulevard Arago, 75014 Paris, France
[49] Max-Planck-Institut für Astronomie, Königstuhl 17, 69117 Heidelberg, Germany
[50] Department of Physics and Helsinki Institute of Physics, Gustaf Hällströmin katu 2, 00014 University of Helsinki, Finland
[51] AIM, CEA, CNRS, Université Paris-Saclay, Université de Paris, 91191 Gif-sur-Yvette, France
[52] Université de Genève, Département de Physique Théorique and Centre for Astroparticle Physics, 24 quai Ernest-Ansermet, CH-1211 Genève 4, Switzerland
[53] Department of Physics, P.O. Box 64, 00014 University of Helsinki, Finland
[54] Helsinki Institute of Physics, Gustaf Hällströmin katu 2, University of Helsinki, Helsinki, Finland
[55] NOVA optical infrared instrumentation group at ASTRON, Oude Hoogeveensedijk 4, 7991PD, Dwingeloo, The Netherlands
[56] Dipartimento di Fisica "Aldo Pontremoli", Università degli Studi di Milano, Via Celoria 16, 20133 Milano, Italy
[57] INAF-IASF Milano, Via Alfonso Corti 12, 20133 Milano, Italy
[58] INFN-Sezione di Milano, Via Celoria 16, 20133 Milano, Italy
[59] Universität Bonn, Argelander-Institut für Astronomie, Auf dem Hügel 71, 53121 Bonn, Germany
[60] Aix-Marseille Université, CNRS, CNES, LAM, Marseille, France
[61] Dipartimento di Fisica e Astronomia "Augusto Righi" - Alma Mater Studiorum Università di Bologna, via Piero Gobetti 93/2, 40129 Bologna, Italy
[62] Department of Physics, Centre for Extragalactic Astronomy, Durham University, South Road, DH1 3LE, UK
[63] Université Côte d'Azur, Observatoire de la Côte d'Azur, CNRS, Laboratoire Lagrange, Bd de l'Observatoire, CS 34229, 06304 Nice cedex 4, France
[64] Université Paris Cité, CNRS, Astroparticule et Cosmologie, 75013 Paris, France
[65] Institut d'Astrophysique de Paris, 98bis Boulevard Arago, 75014, Paris, France
[66] European Space Agency/ESTEC, Keplerlaan 1, 2201 AZ Noordwijk, The Netherlands
[67] School of Mathematics, Statistics and Physics, Newcastle University, Herschel Building, Newcastle-upon-Tyne, NE1 7RU, UK
[68] Department of Physics, Institute for Computational Cosmology, Durham University, South Road, DH1 3LE, UK
[69] Department of Physics and Astronomy, University of Aarhus, Ny Munkegade 120, DK-8000 Aarhus C, Denmark
[70] Waterloo Centre for Astrophysics, University of Waterloo, Waterloo, Ontario N2L 3G1, Canada
[71] Department of Physics and Astronomy, University of Waterloo, Waterloo, Ontario N2L 3G1, Canada
[72] Perimeter Institute for Theoretical Physics, Waterloo, Ontario N2L 2Y5, Canada
[73] Space Science Data Center, Italian Space Agency, via del Politecnico snc, 00133 Roma, Italy
[74] Centre National d'Etudes Spatiales – Centre spatial de Toulouse, 18 avenue Edouard Belin, 31401 Toulouse Cedex 9, France
[75] Institute of Space Science, Str. Atomistilor, nr. 409 Măgurele, Ilfov, 077125, Romania
[76] Instituto de Astrofísica de Canarias, Calle Vía Láctea s/n, 38204, San Cristóbal de La Laguna, Tenerife, Spain
[77] Departamento de Astrofísica, Universidad de La Laguna, 38206, La Laguna, Tenerife, Spain
[78] Dipartimento di Fisica e Astronomia "G. Galilei", Università di Padova, Via Marzolo 8, 35131 Padova, Italy
[79] Departamento de Física, FCFM, Universidad de Chile, Blanco Encalada 2008, Santiago, Chile
[80] Institut d'Estudis Espacials de Catalunya (IEEC), Edifici RDIT, Campus UPC, 08860 Castelldefels, Barcelona, Spain
[81] Institute of Space Sciences (ICE, CSIC), Campus UAB, Carrer de Can Magrans, s/n, 08193 Barcelona, Spain
[82] Satlantis, University Science Park, Sede Bld 48940, Leioa-Bilbao, Spain
[83] Centro de Investigaciones Energéticas, Medioambientales y Tecnológicas (CIEMAT), Avenida Complutense 40, 28040 Madrid, Spain
[84] Instituto de Astrofísica e Ciências do Espaço, Faculdade de Ciências, Universidade de Lisboa, Tapada da Ajuda, 1349-018 Lisboa, Portugal
[85] Universidad Politécnica de Cartagena, Departamento de Electrónica y Tecnología de Computadoras, Plaza del Hospital 1, 30202 Cartagena, Spain
[86] Kapteyn Astronomical Institute, University of Groningen, PO Box 800, 9700 AV Groningen, The Netherlands
[87] INFN-Bologna, Via Irnerio 46, 40126 Bologna, Italy
[88] Infrared Processing and Analysis Center, California Institute of Technology, Pasadena, CA 91125, USA
[89] IFPU, Institute for Fundamental Physics of the Universe, via Beirut 2, 34151 Trieste, Italy
[90] INAF, Istituto di Radioastronomia, Via Piero Gobetti 101, 40129 Bologna, Italy
[91] Centre de Calcul de l'IN2P3/CNRS, 21 avenue Pierre de Coubertin 69627 Villeurbanne Cedex, France
[92] INFN-Sezione di Roma, Piazzale Aldo Moro, 2 - c/o Dipartimento di Fisica, Edificio G. Marconi, 00185 Roma, Italy
[93] Institut für Theoretische Physik, University of Heidelberg, Philosophenweg 16, 69120 Heidelberg, Germany
[94] Université St Joseph; Faculty of Sciences, Beirut, Lebanon
[95] Junia, EPA department, 41 Bd Vauban, 59800 Lille, France
[96] SISSA, International School for Advanced Studies, Via Bonomea 265, 34136 Trieste TS, Italy
[97] INFN, Sezione di Trieste, Via Valerio 2, 34127 Trieste TS, Italy

[98] ICSC - Centro Nazionale di Ricerca in High Performance Computing, Big Data e Quantum Computing, Via Magnanelli 2, Bologna, Italy
[99] Instituto de Física Teórica UAM-CSIC, Campus de Cantoblanco, 28049 Madrid, Spain
[100] CERCA/ISO, Department of Physics, Case Western Reserve University, 10900 Euclid Avenue, Cleveland, OH 44106, USA
[101] Laboratoire Univers et Théorie, Observatoire de Paris, Université PSL, Université Paris Cité, CNRS, 92190 Meudon, France
[102] Dipartimento di Fisica e Scienze della Terra, Università degli Studi di Ferrara, Via Giuseppe Saragat 1, 44122 Ferrara, Italy
[103] Istituto Nazionale di Fisica Nucleare, Sezione di Ferrara, Via Giuseppe Saragat 1, 44122 Ferrara, Italy
[104] Kavli Institute for the Physics and Mathematics of the Universe (WPI), University of Tokyo, Kashiwa, Chiba 277-8583, Japan
[105] Dipartimento di Fisica - Sezione di Astronomia, Università di Trieste, Via Tiepolo 11, 34131 Trieste, Italy
[106] Minnesota Institute for Astrophysics, University of Minnesota, 116 Church St SE, Minneapolis, MN 55455, USA
[107] Institute Lorentz, Leiden University, Niels Bohrweg 2, 2333 CA Leiden, The Netherlands
[108] Institute for Astronomy, University of Hawaii, 2680 Woodlawn Drive, Honolulu, HI 96822, USA
[109] Department of Physics & Astronomy, University of California Irvine, Irvine CA 92697, USA
[110] Department of Astronomy & Physics and Institute for Computational Astrophysics, Saint Mary's University, 923 Robie Street, Halifax, Nova Scotia, B3H 3C3, Canada
[111] Departamento Física Aplicada, Universidad Politécnica de Cartagena, Campus Muralla del Mar, 30202 Cartagena, Murcia, Spain
[112] Department of Physics, Oxford University, Keble Road, Oxford OX1 3RH, UK
[113] Institute of Cosmology and Gravitation, University of Portsmouth, Portsmouth PO1 3FX, UK
[114] Department of Computer Science, Aalto University, PO Box 15400, Espoo, FI-00 076, Finland
[115] Ruhr University Bochum, Faculty of Physics and Astronomy, Astronomical Institute (AIRUB), German Centre for Cosmological Lensing (GCCL), 44780 Bochum, Germany
[116] Univ. Grenoble Alpes, CNRS, Grenoble INP, LPSC-IN2P3, 53, Avenue des Martyrs, 38000, Grenoble, France
[117] Department of Physics and Astronomy, Vesilinnantie 5, 20014 University of Turku, Finland
[118] Serco for European Space Agency (ESA), Camino bajo del Castillo, s/n, Urbanizacion Villafranca del Castillo, Villanueva de la Cañada, 28692 Madrid, Spain
[119] ARC Centre of Excellence for Dark Matter Particle Physics, Melbourne, Australia
[120] Centre for Astrophysics & Supercomputing, Swinburne University of Technology, Victoria 3122, Australia
[121] School of Physics and Astronomy, Queen Mary University of London, Mile End Road, London E1 4NS, UK
[122] Department of Physics and Astronomy, University of the Western Cape, Bellville, Cape Town, 7535, South Africa
[123] ICTP South American Institute for Fundamental Research, Instituto de Física Teórica, Universidade Estadual Paulista, São Paulo, Brazil
[124] Oskar Klein Centre for Cosmoparticle Physics, Department of Physics, Stockholm University, Stockholm, SE-106 91, Sweden
[125] Astrophysics Group, Blackett Laboratory, Imperial College London, London SW7 2AZ, UK
[126] INAF-Osservatorio Astrofisico di Arcetri, Largo E. Fermi 5, 50125, Firenze, Italy
[127] Dipartimento di Fisica, Sapienza Università di Roma, Piazzale Aldo Moro 2, 00185 Roma, Italy
[128] Centro de Astrofísica da Universidade do Porto, Rua das Estrelas, 4150-762 Porto, Portugal
[129] Dipartimento di Fisica, Università di Roma Tor Vergata, Via della Ricerca Scientifica 1, Roma, Italy
[130] INFN, Sezione di Roma 2, Via della Ricerca Scientifica 1, Roma, Italy
[131] Institute of Astronomy, University of Cambridge, Madingley Road, Cambridge CB3 0HA, UK
[132] Department of Astrophysics, University of Zurich, Winterthurerstrasse 190, 8057 Zurich, Switzerland
[133] Dipartimento di Fisica, Università degli studi di Genova, and INFN-Sezione di Genova, via Dodecaneso 33, 16146, Genova, Italy
[134] Theoretical astrophysics, Department of Physics and Astronomy, Uppsala University, Box 515, 751 20 Uppsala, Sweden
[135] Department of Physics and Astronomy, University College London, Gower Street, London WC1E 6BT, UK
[136] Department of Astrophysical Sciences, Peyton Hall, Princeton University, Princeton, NJ 08544, USA
[137] Niels Bohr Institute, University of Copenhagen, Jagtvej 128, 2200 Copenhagen, Denmark
[138] Cosmic Dawn Center (DAWN)
[139] Center for Cosmology and Particle Physics, Department of Physics, New York University, New York, NY 10003, USA
[140] Center for Computational Astrophysics, Flatiron Institute, 162 5th Avenue, 10010, New York, NY, USA

Appendix

In this appendix, we provide detailed computations for determining the variance of the observable $\hat{o}_\ell$. We begin by defining the estimator $\hat{a}_{\ell m,\mathrm{sp}}$ for the spectroscopic survey as $\hat{a}_{\ell m,\mathrm{sp}} = b_{\mathrm{sp}} a^{\mathrm{DM}}_{\ell m} + a^{p}_{\ell m,\mathrm{sp}}$, where b_{sp} represents the spectroscopic bias, assumed to be a constant (i.e. no stochasticity in the bias) $a^{DM}_{\ell m}$ denotes the contribution from the matter distribution, and finally $a^{p}_{\ell m,\mathrm{sp}}$ represents the contribution from the Poisson noise. For simplicity, we initially consider a full sky scenario ($f_{\mathrm{sky}} = 1$). The Poisson noise is characterized by $\left\langle a^{p}_{\ell m,\mathrm{sp}} \right\rangle = 0$ and $\left\langle \left| a^{p}_{\ell m,\mathrm{sp}} \right|^2 \right\rangle = \frac{1}{n_{\mathrm{sp}}}$. The estimator of the angular power spectrum is given by

$$\widehat{C}_{\ell,\mathrm{sp}} = \frac{1}{2\ell+1} \sum_m \left| \hat{a}_{\ell m,\mathrm{sp}} \right|^2 = \frac{1}{2\ell+1} \sum_m \left(b^2_{\mathrm{sp}} \left| a^{\mathrm{DM}}_{\ell m} \right|^2 + 2 b_{\mathrm{sp}} \mathrm{Re}(a^{\mathrm{DM}}_{\ell m} a^{p\,*}_{\ell m}) + \left| a^{p}_{\ell m} \right|^2 \right) . \tag{.34}$$

The average over Poisson realization yields

$$\left\langle \widehat{C}_{\ell,\mathrm{sp}} \right\rangle = \frac{1}{2\ell+1} \sum_m b^2_{\mathrm{sp}} \left| a^{\mathrm{DM}}_{\ell m} \right|^2 + \frac{1}{n_{\mathrm{sp}}} = \overline{C}_{\ell,\mathrm{sp}} + \frac{1}{n_{\mathrm{sp}}} . \tag{.35}$$

Here, the quantity $\overline{C}_{\ell,\mathrm{sp}}$ is introduced. For the photometric survey, similar expressions can be formulated, with the Poisson noise being negligible due a significantly larger n_{ph} compared to n_{sp}. Consequently, for the photometric angular power spectrum, we have

$$\left\langle \widehat{C}_{\ell,\mathrm{ph}} \right\rangle \simeq \overline{C}_{\ell,\mathrm{ph}} = \frac{1}{2\ell+1} \sum_m b^2_{\mathrm{ph}} \left| a^{\mathrm{DM}}_{\ell m} \right|^2 . \tag{.36}$$

The observable $\hat{o}_\ell$ can then be expressed as

$$\hat{o}_\ell = \frac{\widehat{C}_{\ell,\mathrm{sp}}}{\widehat{C}_{\ell,\mathrm{ph}}} \simeq \frac{\widehat{C}_{\ell,\mathrm{sp}}}{\overline{C}_{\ell,\mathrm{ph}}} = \left(\frac{b_{\mathrm{sp}}}{b_{\mathrm{ph}}} \right)^2 + \frac{1}{(2\ell+1)\overline{C}_{\ell,\mathrm{ph}}} \sum_m \left(2 b_{\mathrm{sp}} \mathrm{Re}(a^{\mathrm{DM}}_{\ell m} a^{p\,*}_{\ell m}) + \left| a^{p}_{\ell m} \right|^2 \right) . \tag{.37}$$

Hence the mean value of this estimator is given by

$$\langle \hat{o}_\ell \rangle = \left(\frac{b_{\mathrm{sp}}}{b_{\mathrm{ph}}} \right)^2 + \frac{1}{n_{\mathrm{sp}} \overline{C}_{\ell,\mathrm{ph}}} . \tag{.38}$$

The variance is then derived from $\sigma^2_o(\ell) = \left\langle (\hat{o}_\ell - \langle \hat{o}_\ell \rangle)^2 \right\rangle$. Using the property $a^*_{\ell m} = (-1)^m a_{\ell,-m}$ and applying the Isserlis' theorem to compute $\left\langle \left| a^{p}_{\ell m} \right|^2 \left| a^{p}_{\ell m'} \right|^2 \right\rangle$ (assuming Isserlis' theorem valid for the Poisson noise), straightforward calculations lead to

$$\sigma^2_o(\ell) = \frac{2}{(2\ell+1) f_{\mathrm{sky}} n_{\mathrm{sp}} \overline{C}^2_{\ell,\mathrm{ph}}} \left(2\overline{C}_{\ell,\mathrm{sp}} + \frac{1}{n_{\mathrm{sp}}} \right) .$$

Here, the f_{sky} factor has been incorporated, and one recovers expression Eq. (23).